FACULTY
OF MATHEMATICS
AND PHYSICS
Charles University

MASTER THESIS

Bc. Maximilián Goleňa

Detection of quantized vortices in the zero temperature limit using silicon/superconducting microwires

Faculty of Mathematics and Physics

Supervisor of the master thesis:	doc. RNDr. David Schmoranzer, Ph.D.
Study programme:	Physics of Condensed Matter and Materials
Study branch:	Low Temperature Physics

Prague 2023

I declare that I carried out this master thesis independently, and only with the cited sources, literature and other professional sources. It has not been used to obtain another or the same degree.

I understand that my work relates to the rights and obligations under the Act No. 121/2000 Sb., the Copyright Act, as amended, in particular the fact that the Charles University has the right to conclude a license agreement on the use of this work as a school work pursuant to Section 60 subsection 1 of the Copyright Act.

In . . . . date . . . .

Author's signature

i

Title: Detection of quantized vortices in the zero temperature limit using silicon/superconducting microwires

Author: Bc. Maximilián Goleňa

Department of Low Temperature Physics: Faculty of Mathematics and Physics

Supervisor: doc. RNDr. David Schmoranzer, Ph.D., Department of Low Temperature Physics

Abstract: In this Thesis, we have characterized and used Microscopic Electrical Mechanical Oscillators (MEMS) in the study of quantum turbulence. Experiments were conducted in the temperature range of 20-920 mK in vacuum in various magnetic fields and in superfluid helium at temperature 20 mK. Resonance properties of MEMS in vacuum showed nonlinear behavior. Low drive peaks showed frequency softening, and high drive peaks showed frequency hardening. We showed that the origin of non-linear behavior lies in the geometry of MEMS. We have shown that our devices are superconductive in field 12.6 mT and is resistive for higher fields. Resonance properties of MEMS do not significantly change with magnetic fields in range 37.8-504 mT. We shown that the motion of MEMS in superfluid helium is highly damped and all measured points were already in turbulent state. MEMS devices can be used to generate quantum turbulence or as its' highly effective local probe.

Keywords: superfluid helium, quantum turbulence, MEMS

Obsah

1

Introduction

Following the liquefaction of helium gas by H.K. Onnes in 1908, the examination of its properties at different temperatures became a logical course of study. The equilibrium phase diagram of Helium is shown in Fig. 1. This diagram differs from the common one as it lacks a triple point, and helium can solidify only at very high pressures. Another discrepancy with helium was discovered in an experiment by Soviet scientist P.L.Kapitsa. He studied the inflow of liquid ^{4}He between two glass discs[2] and he observed a sudden flow rate increase after reaching the critical temperature of 2.17 K. This experiment is noted as a discovery of the superfluid phase of liquid helium. In the same year American team of Allen and Misener [3] conducted similar experiment and they discovered the same thing. Although Kapitza is acknowledged for this discovery, there exists a widespread belief that it should be attributed to all three scientists involved.

Superfluid helium, historically He II, shows even more interesting properties, such as inviscid flow and zero entropy. Temperature dependence of its heat capacity, Figure 2, shows a sudden spike for the temperature of 2.17 K and is similar to the greek letter λ. This leads to the naming convention of transition temperature as λ - temperature. This shape is one of the signs that the transition to the superfluid phase is second order transition, carries no latent heat and can be described by Landau theory.

Even though He II was discovered in 1938, developing a generally approved theoretical description took years. On one side was L. Tisza, who proposed that He II atoms, set on their base energy level and create Bose-Einstein condensate. Consequently, helium atoms cannot dissipate energy, so they move without viscosity and carry no entropy. On the other side stood L.D. Landau, who argued that He II atoms could not undergo Bose-Einstein condensation. Landau's assertion
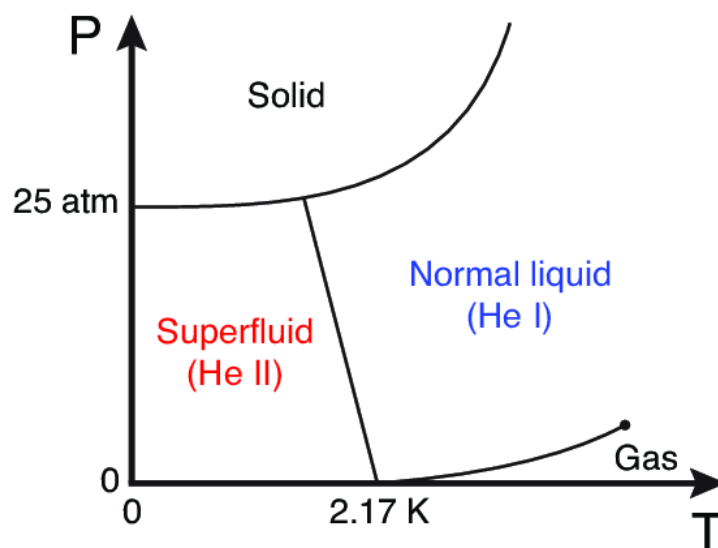
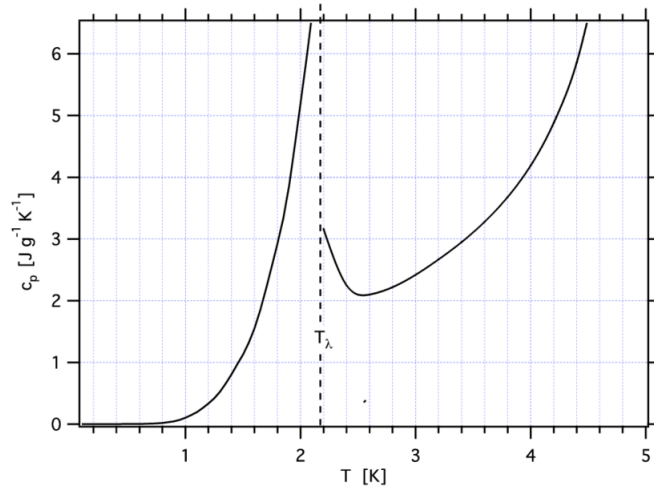

Fig. 1: Phase diagram of ^{4}He[1].

Fig. 2: Heat capacity of liquid helium [4]

was based on the notion that the interaction between helium atoms, which cannot be neglected, contradicts the primary requirement for condensation. He proposed the idea of thermal excitation of He II atoms, which he described by introducing quasiparticles rotons and phonons. Experiments showed that both descriptions were partially correct and used in unison.

One of the most studied topics in the research of superfluidity is quantum turbulence [5]. This phenomenon shows some similarities to classical turbulence, which we experience daily, but differs on a fundamental level. For example, the circulation of classical vortices shows continuous circulation, but all quantised vortices have the same quantised circulation. This phenomenon holds true due to the fact that this is the most energy-favourable arrangement.

Mechanical oscillators are commonly used to study quantum turbulence because they provide a local view of this phenomenon. They are usually small devices, i.e., quartz tuning forks or superconducting wires placed in a magnetic field. They show resonance behaviour that depends on the state of the fluid. For example, in the presence of vortices, the effective damping is higher, which lowers the amplitude and broadens the resonance peak. These devices can even be used to measure He II's material properties, such as the normal fluid density, pressure and viscosity [6] or at high driving force to generate turbulence around them.

Another unique feature of He II is the existence of different sound modes; in addition to classical pressure wave (*first sound*), the waves of entropy (*second sound*) are present. Attenuation of second sound wave on quantised vortices is commonly used as another probe of quantum turbulence [7].

Superfluidity is not a phenomenon only limited to ^{4}He, but it is observed even in ^{3}He. The critical temperature for superfluid ^{3}He is in the range of milikelvin and is dependent on the external magnetic field. The fermionic character of its nuclei causes these differences. This shows that the origin superfluidity in ^{3}He is more similar to conventional superconductors, where the Cooper pairs are created.

3

1. Theoretical background

This thesis will primarily focus on the examination and analysis of application of fluid dynamics,which is part of the physics of continuum. Continuum can be defined as medium that still contains many molecules even after considering infinitesimally small volume. There are two basic approaches to fluid dynamics. In the Lagrangian description, we follow one particle moving in the flow vector field. In Eulerian description, we consider a particular regionin the volume of the fluid and study it's flow, i.e. velocity field is dependent on the time and position $\mathbf{v}(\mathbf{x},t)$. In this work, we will be using the lather description. As we will see in Section 1.2.1 to describe the dynamics of the quantum liquid, one may begin with the dynamics of classical fluids.

1.1   Classical fluid dynamics

One of the fundamental laws in fluid dynamics is the equation of continuity

$$\frac{\partial \rho}{\partial t} + \nabla\dot{(}\rho\mathbf{v}) = 0. \tag{1.1}$$

This equation illustrates that if the density ρ increases with time, It leads to flow outwards from the enclosed area. The product of the fluid's velocity $\mathbf{v}$ and its density carry the meaning of mass flux density. Overall, Equation 1.1 convey the equivalent meaning as the law of conservation of mass in the fluid. This equation holds true in general. In the following description, we assume that fluid is incompressible, meaning the fluid's density is constant with respect to time. It follows that the equation of continuity reduces to a simplified form

$$\nabla \cdot v = 0.. \tag{1.2}$$

In the context of potential flows, energy is an additional property that is conserved. This fact is shown in Bernoulli's Equation

$$p + \frac{1}{2}\rho v^2 = const \tag{1.3}$$

The first term represents potential energy caused by the pressure p, and the second term is the kinetic energy of the fluid. This equation holds only for isothermal flow.

Euler's equations describe the flow of incompressible ideal fluid

$$\frac{\partial \mathbf{v}}{\partial t} + (\mathbf{v} \cdot \nabla)\mathbf{v} = -\frac{\nabla p}{\rho} \tag{1.4}$$

The right side of Equation 1.4 represents the pressure force in the liquid. On the other hand, the left side is in a unit of acceleration. Hence, it can be deduced that Euler's equation embodies a form of Newton's second law of mechanics.

Euler's equation is valid exclusively for ideal fluid, where the fluid's motion remains unaffected by any dissipative forces. Adding viscous dissipative force, we obtain Navier-Stokes equations

$$\frac{\partial \mathbf{v}}{\partial t} + (\mathbf{v} \cdot \nabla)\mathbf{v} = -\frac{\nabla p}{\rho} + \nu\Delta\mathbf{v} \tag{1.5}$$

in which ν stands for kinematic viscosity. These equations represent a system of nonlinear equations for each component of velocity field $\boldsymbol{v}$. In the case of compressible fluids, the form of these equations becomes more complex.

To achieve complete information of the dynamics of the system, it is necessary to solve both equation of continuity and the Eqs. 1.4 or 1.5.

An alternative approach to describing fluid dynamics involves utilizing dimensionless parameters, i.e. Reynolds, Mach or Nusselt number[1]. Which of these parameters will be used depends on the problem. Probably the most common dimensionless parameter is the Reynolds number, which can be derived from the Navier-Stokes equation by introducing the dimensionless equivalent of the physical quantities

$$\mathbf{v'} = \frac{\mathbf{v}}{U}, \ \ \nabla' = D\nabla \tag{1.6}$$

using characteristic velocity U of the flow and D is characteristic dimension. The latter parameter is highly dependent on the geometry of the problem, i.e., for flow in the long channel, it would be the diameter of the channel. There are two possible choices for the definition of dimensionless pressure p'. In the case of dominant inertia forces, p' is defined as a) and vice versa.

$$a) \ p' = \frac{p}{\rho U}, \ \ b) \ p' = \frac{D}{\nu U}p \tag{1.7}$$

From that, we get the definition of the Reynolds number

$$Re = \frac{vD}{\nu}, \tag{1.8}$$

which is used to describe the state of the flow. Three distinct regimes may be observed. In laminar flow, fluid particles move across the non self-intersecting smooth lines. In this state, the velocity of the fluid is relatively small, from which follows that the Reynolds number is also small. In the following regime flow is in transition to turbulent state, which, in circular pipes, happens for Re $\approx$ 1000 [8]. For high velocities and Reynolds number is the fluid in a fully developed turbulent regime[2]. Even though the rigorous description of turbulence does not exist, in the next Section, we will describe the basic concept of the phenomenological Kolmogorov turbulence theory.

1.1.1 Phenomenological description of turbulence

In this Section, we will consider only the viscous fluids which satisfy Navier-Stokes equations 1.5. Turbulent flows only occur for high Reynolds numbers and show chaotic behaviour. From that follows the replacement of the deterministic description with statistical analysis. Turbulent flows are highly diffusive, which implies a high spread of velocity fluctuation. Phenomenological Kolmogorov's (K41) theory [9] assumes local isotropy and homogeneity This theory is limited

---

[1]Mach number is defined as local flow velocity u to the local speed of sound c.It can be used to study wave propagation in the fluid and study different flow regime, i.e., subsonic or supersonic. Nusselt number is used in describing convective flows and is defined as the ration of convective and conductive heat transfer.

[2]Flow around the sphere is turbulent for Re $\approx$ 4000 [8]

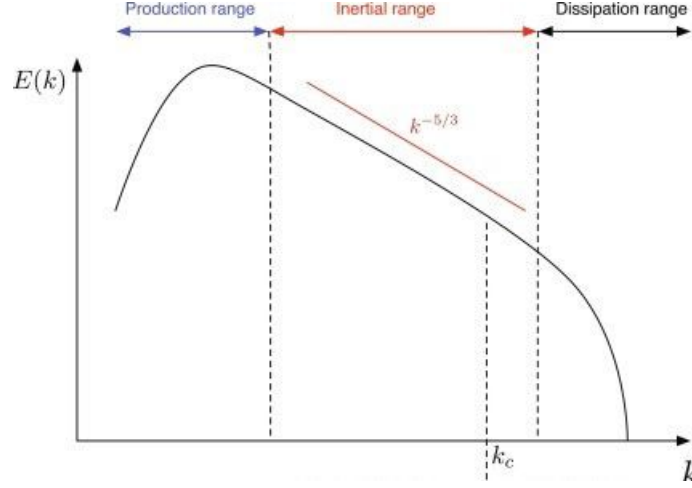Fig. 1.1: k-dependence of energy spectrum of the turbulent flow [10]

uniquely to 3D turbulence. These assumptions, with the viscous nature of the fluid, lead to the dissipation of the turbulent energy

$$\epsilon = \nu \langle \omega^2 \rangle \tag{1.9}$$

where circulation ω is $\nabla \times \mathbf{v}$.

Assuming turbulence generated by an external force, i.e., a grid's motion, the flow's energy spectrum can be described at three different length scales. The production range gives rise to significant eddies resulting from instabilities associated with high Reynolds numbers. Due to the equipartition theorem, they show k^2 dependence on their wave vector k. Upon reducing the motion of the grid, the eddies will commence a process of decay, with no dissipation of energy occurring. Eddies do not dissipate energy because their motion is too unstable, and molecular viscosity is not effective enough in dissipating their turbulent kinetic energy. In this *inertial range*, the Kolmogorov's theory predicts famous k-dependence of energy spectrum as

$$E(k) \propto \epsilon^{2/3} k^{-5/3} \tag{1.10}$$

Only eddies in the Kolmogorov length scales

$$\eta = (\nu^3/\epsilon)^{\frac{1}{4}} \tag{1.11}$$

dissipate energy. The whole process, from the generation of large eddies to dissipating eddies in Kolmogorov's length scale eddies, is known as the Richardson cascade and is shown in Figure 1.2. This phenomenon shows that unless the turbulent flows constantly receive energy from an outside source, vortices will rapidly decay and turn into the laminar flow.
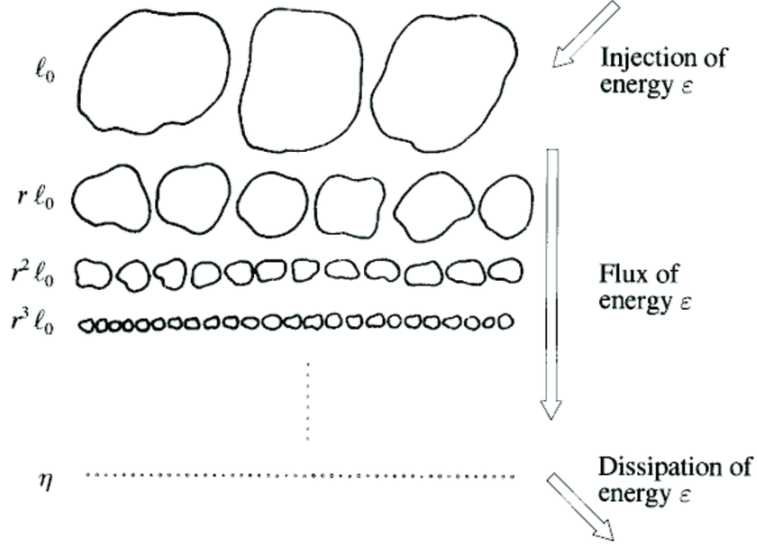
Fig. 1.2: Richardson cascade [11]

1.1.2 Boundary layers

A relatively common interest of fluid dynamics is the flow around the solid body submerged in the fluid. It can be either wing of the plane in the air or our mechanical oscillator in the superfluid helium. When the submerged body undergoes a motion, due to viscous force it carries portion of the fluid with it. This is called the boundary layer. On the other hand, at location far from the body viscous forces are not sufficiently strong to affect the flow. In this region, the flow can be approximately described by Bernoulli's Equation 1.3.

Blasius' boundary layer

In this Section, we will take a closer look at the boundary layer and assume stationary flow, $\partial v / \partial t = 0$. In the immediate vicinity of the body, the no-slip boundary conditions of the Navier-Stokes equation manifest. This condition states that the fluid's velocity has to be zero at the body's solid walls. From that follows, the velocity field must decrease in the proximity of the wall. The fluid's motion, in Blasius' boundary layer, cannot be described by Equation 1.5; instead one need to use Prandtls' equations

$$v_x \frac{\partial_x}{\partial x} + v_y \frac{\partial_y}{\partial x} - \nu \frac{\partial^2 v_x}{\partial y^2} = -\frac{1}{\rho}\frac{dp}{dx} = U \frac{dU}{dx} \tag{1.12}$$

$$\frac{\partial v_x}{\partial x} + \frac{\partial v_y}{\partial y} = 0 \tag{1.13}$$

These two equations are only written in two dimensions because the motion of the fluid takes place mainly parallel to the surface. Prandtls' equations assume no transverse pressure gradient in the boundary layer.

As discussed in Section 1.1 with flows with high Reynold's number the flow is in turbulent state. The same holds true in the boundary layer. At higher fluid

Fig. 1.3: Separation of boundary layer around the airfoil [12]

velocities, flow transitions to a turbulent state, where it is highly chaotic and full of vortices. If the boundary layer flow is met with a strong pressure gradient in a different direction, the boundary layer is separated at *separation line*. The shape and behaviour of the boundary layer are highly dependent on the body's shape. The boundary layer around the airfoil is shown in Fig. 1.3.

Stokes' boundary layer

In this Section, we will describe flow around the oscillating bodies. Let's consider infinite plane harmonically oscillating with frequency[3] ω. The velocity field in the boundary layer decreases exponentially at the length scale of δ_s, commonly called depth of penetration.

$$v = v_0 \, e^{-x/\delta_s} \, e^{i(x\delta_s - \omega t)} \tag{1.14}$$

$$\delta_s = \sqrt{\frac{2\nu}{\omega}} \tag{1.15}$$

In these equations, v_0 represents an amplitude of the velocity field, and t is time. The time evolution of the velocity field is shown in Figure 1.4, where the time interval is 0.1 s, and the colour tone represents time evolution of the movement. This is known as Stokes's second problem of fluid dynamics.

1.1.3 Drag forces

In the previous Section, we discussed flow in the boundary layer.However, we have yet to address the inverse query: How does the flow affect the body? The movement of the body is slowed down by dissipative drag force. To define this force, one must clarify whether the flow is laminar or turbulent. In turbulent flow, the body interacts with more eddies, which results in higher drag force. In the

---
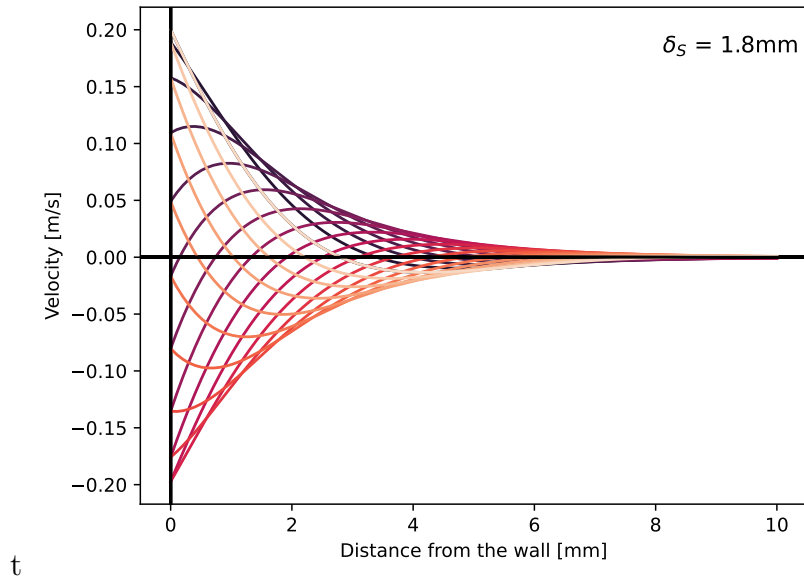
[3]Detailed derivation is provided in [13] at pages 83-85

Fig. 1.4: Evolution of spanwise velocity on Stokes' boundary layer. The light yellow line indicates the velocity profile for t=0, and the time evolution is shown in gradually darker colours.
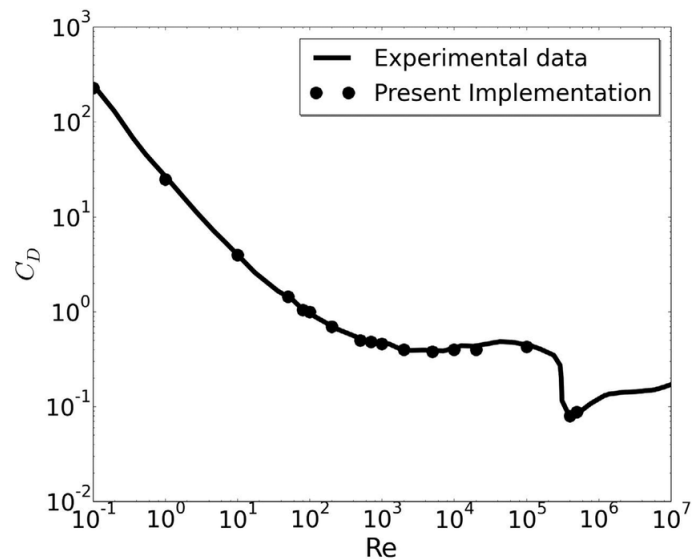

Fig. 1.5: Dependancy of drag coeficient C_D on Reynolds number Re for flow around the sphere [14].

purely laminar flow, the viscous drag forces are proportional to the velocity

$$F \propto bv \tag{1.16}$$

and in turbulent flow

$$F_D = \frac{1}{2}\rho v^2 C_D A. \tag{1.17}$$

Drag depends on the cross-section area perpendicular to flow direction A and dimensionless drag coefficient C_D. To describe the dependence of the drag coefficient on the flow, it is helpful to discuss relationship between drag coefficient and Reynold's number,see Figure.1.5. This Figure can be divided into three regions. As the Reynolds numbers increase within the range of 0 to 10^2, the drag coefficient exhibits a linear decrease. These low Reynolds numbers imply fully laminar state of flow. While the Reynolds number is increasing, the wake is the transition to a turbulent state. Upon the attainment of fully developed turbulence in the wake, a plateau is observed. The drag coefficient sharply decreases at the Reynolds number $\approx 10^6$. This can be explained by the fact that laminar boundary layers have higher boundary layer thickness. This leads to sooner separation of flow from the body than in turbulent state. As a consequence there is a lower wake behind the body and, thus, lower drag. This effect is know as a drag crisis.

Another property impacting the drag coefficient is the shape of the body. A lower drag coefficient indicates lower aerodynamic drag. This fact is commonly used in improving the aerodynamic design of wings for planes.

1.2 Superfluid helium, quantum fluid dynamics

Below the critical temperature of $T_\lambda = 2.17K$ at SVP, saturated vapour pressure, liquid helium undergoes a second-order transition to the superfluid phase. Superfluid helium shows quantum properties on a macroscopic scale, which leads to the necessity of quantum-mechanical description. Helium can be described as an ideal gas with small interaction that, under the critical temperature T_λ, undergoes Bose-Einstein condensate [4].

A macroscopic wave function describes superfluid helium

$$\psi(\mathbf{r}, t) = \psi_0 e^{i\Phi(\mathbf{r},t)} \tag{1.18}$$

where $\mathbf{r}$ is the space vector, Ψ is the macroscopic phase and $\psi_0 = \sqrt{\rho_s/m_4}$ is the amplitude, which is function of superfluid phase density and the mass of the ^{4}He atom. This wave function is defined for the whole condensate, which explains the helium atoms' coherent behaviour.

1.2.1 Two-fluid model

In 1946, Landau proposed the experiment to E.L.Andronikashvili, which lead to a new view on superfluid helium. In the experiment, he put very closely packed disc torque oscillators on the wire, applied torque force and measured the angular

---

[4]Without the interaction among the helium atoms, the Bose-Einstein condensation wouldn't be possible [15]
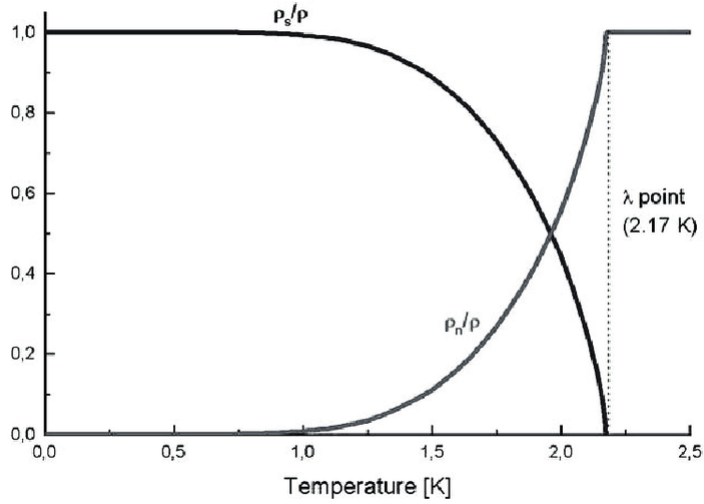
b

Fig. 1.6: Temperature dependence of normal and superfluid component of He II [16]

velocity of his apparatus. The surprising result arose after decreasing the temperature, which led to an increase in resonant frequency [17]. From this result, he induced that He II contains two separate components, normal and superfluid. Both of these components carry their density, and they sum to the total density of the whole liquid

$$\rho = \rho_n + \rho_s. \tag{1.19}$$

The resonant frequency increase can be attributed to the dependence of the component's density on temperature, Fig. 1.6. Normal and superfluid components are mutually independent unless quantised vortices are present in He II. This links them via mutual friction force F_{ns}.

Dynamics of normal and superfluid components are described with HVBK equations [18]

$$\frac{\partial \mathbf{v}_s}{\partial t} + (\mathbf{v}_s \cdot \nabla) \mathbf{v}_s = -\frac{1}{\rho} \nabla p + s \nabla T + \mathbf{T} - \frac{\rho_n}{\rho} \mathbf{F}_{ns} \tag{1.20}$$

$$\frac{\partial \mathbf{v}_n}{\partial t} + (\mathbf{v}_n \cdot \nabla) \mathbf{v}_n = -\frac{1}{\rho} \nabla p - \frac{\rho_s}{\rho_n} s \nabla T + \nu_n \Delta \mathbf{v}_n + \frac{\rho_s}{\rho} \mathbf{F}_{ns} \tag{1.21}$$

where $\mathbf{v_i}$ is the velocity of an individual component, s is a specific entropy of the system, $\boldsymbol{T}$ is the tension force[5] which describes changes in shape and form of quantised vortices. If the flow is isotropic and without the presence of quantum vortices HVBK equation transition to Euler's 1.4 and Navier-Stoke's1.5, therefore superfluid component can be considered as an analogy to ideal fluid and normal component to classical, viscous fluid.

---

[5]In classical fluid mechanics exists similar quantity called vortex stretching and $\nu_n = \eta \ / \ rho_n$ is the kinematic viscosity of normal component. The flow lengthens Eddies due to the law of conservation of angular momentum.
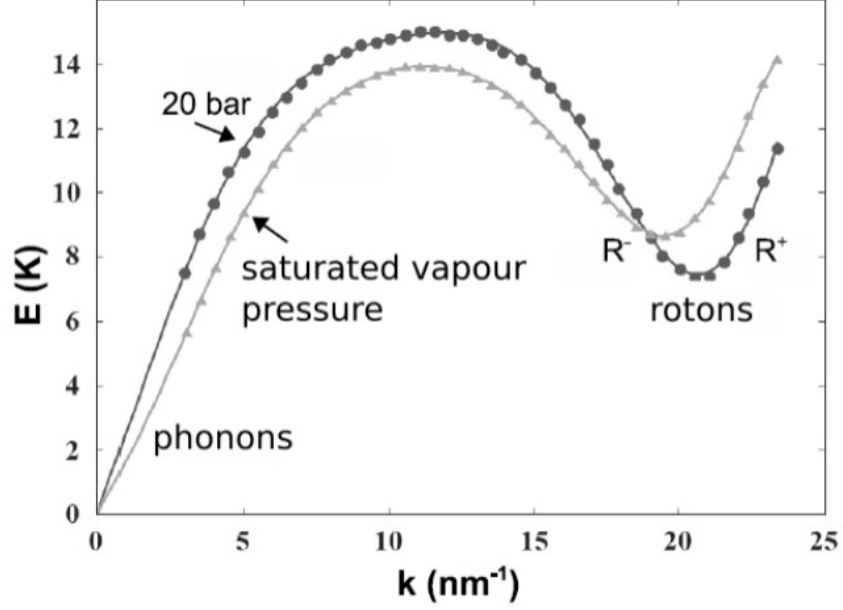
Fig. 1.7: Dispersion curve of in He II [15].

This theory provides only a phenomenological description of superfluid helium. A more accurate perspective would involve considering He II as a superposition of the normal state and the superfluid state, rather than as comprising two distinct entities..

1.2.2 Microscopic description of He II

First microscopic description of He II was firstly introduced L.D.Landau. He described the interaction between helium atoms as quasiparticles, which behave as perturbations of the ideal non-interactive state. In addition to that, Landau proposed the dispersion curve of these quasiparticles, shown in Fig 1.7. The dispersion curve begins with the long-wave phonon part, which can be described by Debye law

$$\epsilon = pc \tag{1.22}$$

where ϵ is energy of quasiparticle, p is its momentum and c is the speed of sound. Following that, the roton minimum is seen, which is described by

$$\epsilon = \Delta + \frac{p^2}{2\mu} \tag{1.23}$$

where μ is the effective mass of the roton [19] and Δ represents roton energy gap. Probably the grates success of Landau's theory is the introduction of critical velocity v_L. He states that if the He II flows faster than

$$v_L = \left[\frac{\epsilon(p)}{p}\right]_{min} \tag{1.24}$$

the quasiparticles will generate in the liquid. This excitations lead to the annihilation of superfluidity and transition to the normal phase.

Experiments show that for high temperatures, the roton part plays a dominant role in heat capacity [20]. The roton energy gap Δ significantly rise under the temperature of the 1 K. Consequently, the contribution of the rotonic component can be disregarded or considered negligible.

1.2.3 Quantum Turbulence

Similar to turbulence in a classical viscous fluid in He II exists a phenomenon known as quantum turbulence, see Fig. 1.8. Quantized vortices are always present in superfluid helium and belong among the most interesting and studied problem of quantum fluids. In the following Section, we provide a short introduction to them.

In Section 1.1.1, we described the turbulence in classical fluids. The difference between classical turbulence and turbulence in He II can be shown by calculating the circulation of He II

$$\Gamma = \oint_c v_s \cdot dr.$$

(1.25)

While integrating along the curve c, the integral has two possible solutions. Considering simple-connected fluid region, we can use Stokes' Theorem to reduce the integral to 0. If the region is not simple-connected, Stokes' Theorem can't be applied.

$$\Gamma = \oint_c v_s dr = \frac{\hbar}{m} \oint_c \nabla\Phi \cdot dr$$

(1.26)

where superfluid velocity has been obtained from momentum operator ($\hat{p} = m\hat{v} = -i\hbar\nabla$ on wave function ψ. From the periodicity of macroscopic phase Φ, we see that the phase difference between starting and final point along the curve
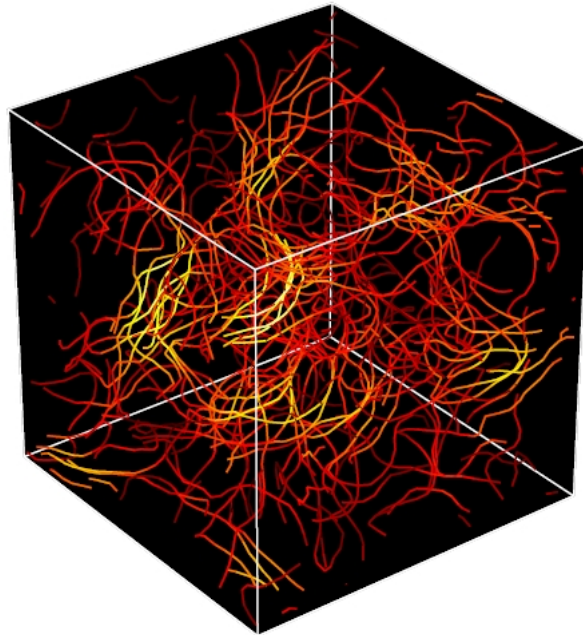

Fig. 1.8: Quantum turbulence computed using vortex filament method [21]

c must be $2\pi q$. Comparing this result with Equation 1.26 we get

$$\Gamma = \frac{h}{m}q = \kappa q. \tag{1.27}$$

where $\kappa = 9.97 \times 10^{-8}$ m²/s is quantum of circulation. This leads to topological defects, quantised vortices, in which the superfluid component flows around vortex core. Vortex core is in normal state. Quantised vortices are formed spontaneously during the superfluid phase transition or are generated by adding an external velocity field.

Classical vortices lose energy due to the viscous nature of the flow. Under T = 1 K He II is almost pure superfluid which leads to increase of the stability of vortex cores. However, this is different for quantised vortices, as waves were observed on them. This phenomenon is known as Kelvin waves [22, 23]. The Cascade of Kelvin waves is a dissipative process and leads to increased length of vortex lines. If this effect is continually driven, it may lead to the reconnection of individual vortices into a tangle of quantised vortices, called quantum turbulence. Vortex line density L, defined as length of vortex line normalized to unit volume, is property commonly used to describe intensity of quantum turbulence. Vortex line density is usually measured by attenuation of second sound[6], where the amplitude a of standing wave is attenuated on quantized vortices to value a_0 and L is obtained using

$$L = \frac{6\pi \Delta f_0}{B\kappa}\left(\frac{a_0}{0} - 1\right) \tag{1.28}$$

where B is the inner friction and Δf_0 is width of original resonance peak. For details see [7].

1.2.4   Mechanical oscillators in He II

This Section will discuss commonly used probes of turbulence and mechanical oscillators. Among the most commonly used are superconducting wires in semi-circular shape [24], quartz tuning fork [25], oscillating grids [26], or oscillating microspheres [27]. The oscillator moves in a medium which damps its movement. In the first description, we can consider only damping linear with the velocity of the oscillator. Constant determining damping in the fluid is commonly denoted as Γ. The restoring force affects the motion, determined by the k. To describe the motion of the oscillator, we can combine all the previous forces mentioned above with Newton's second law of mechanics and get

$$m\frac{d^2x}{dt^2} + \Gamma\frac{dx}{dt} + kx = Fe^{i\omega t}. \tag{1.29}$$

This is the equation of a damped linear harmonic oscillator driven with force with the amplitude F and angular frequency ω. The solution can be found in the form

$$u = \hat{u}_0 e^{i\omega t} \tag{1.30}$$

where the complex amplitude $\hat{u}_0$ is

$$Re\{\hat{u}_0\} = \frac{F}{m}\frac{\gamma\omega^2}{(\omega_0^2 - \omega^2)^2}, \; Im\{\hat{u}_0\} = \frac{F}{m}\frac{\omega(\omega_0^2 - \omega^2)^2}{(\omega_0^2 - \omega^2)^2} \tag{1.31}$$

---

[6]Second sound is wave mode unique for He II where the superfluid and normal phase is oscillating out-of phase.
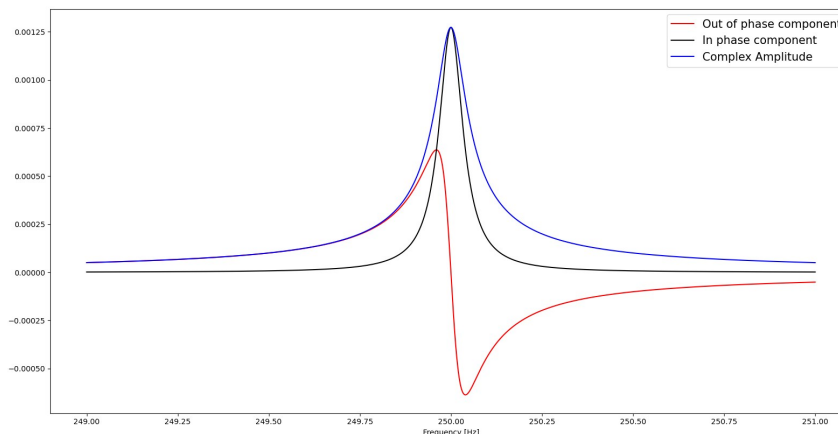
Fig. 1.9: Complex amplitude of velocity of the linear harmonic oscillator. The black line shows an in-phase amplitude component, and the red line represents a velocity shifted by 90 degrees.

in which $\gamma = \Gamma/m$ and $\omega_0 = \sqrt{k/m}$. This is Lorentz curve and is shown in Fig. 1.9. The resonance behavior of the oscillator is affected by the damping coefficient, which broadens the resonance peak. The width of the peak can be found either as Full Width at Half Maximum (FWHM) of the in-phase component (black curve) or as a difference in frequencies of maximum and minimum of the out-of-phase component (red curve).

To describe more complex behavior, non-linear models of oscillators are used. They are described by Duffing's equation

$$\frac{d^2x}{dt} + \gamma\frac{dx}{dt} + \alpha_1 x + \alpha_3 x^3 = f cos(\omega t) \tag{1.32}$$

in which α_1 represents a coefficient of linear restoring force and α_3 is a coefficient of cubic restoring. This equation is just an extension of Equation 1.29 with another non-linear restoring force. The duffing equation does not have an explicit analytical solution, but the implicit solution for the complex amplitude can be found in [28]. This equation has three solutions, one for the linear case $\alpha_3 = 0$, and one for positive and negative α_3. These solutions are shown in the Fig. 1.10

The experimental use of mechanical oscillators is based on their interaction with the fluid flow. The motion of the resonators is damped by viscous forces, resulting in a decrease in amplitude and a broadening of the width of the resonance peak. By introducing external flow or turbulence, the dampening of the resonance peak is even stronger. Thanks to that, mechanical oscillators can be used as a local probe of the quantum turbulence [24]. This method will be further discussed in Section 2.3.
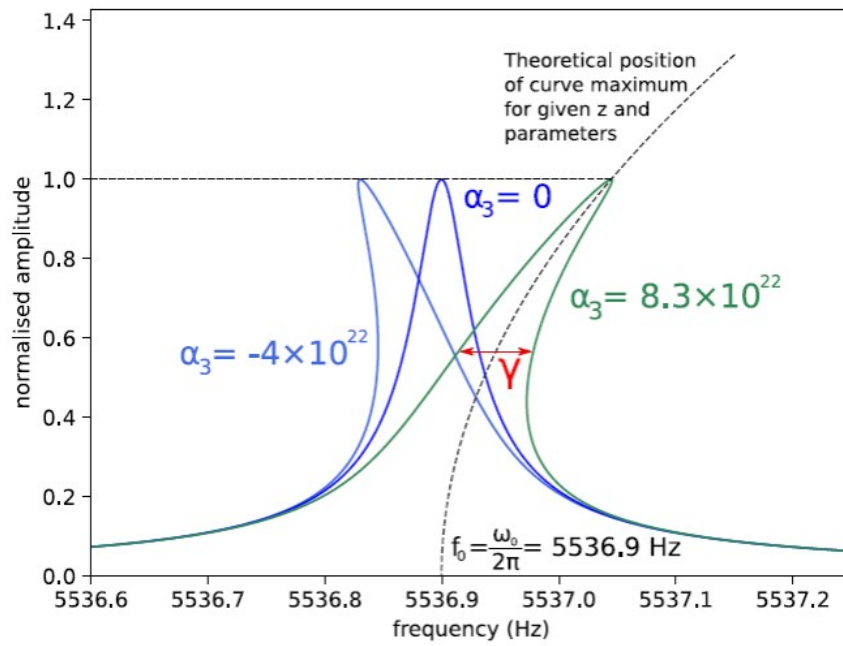
Fig. 1.10: Solution of Duffing equation for three different parameter values α_3. The dark blue line represents linear solution $\alpha_3 = 0$; the green line represents a curve with positive cubic restoring force $\alpha_3 > 0$ and light blue for negative restoring force. Similarly to the linear case, coefficient gamma correlates with FWHM of the resonance curve [28].

2. Experimental apparatus

Experiments were conducted in a standard helium bath cryostat. In order to observe the surface level of liquid helium within a dewar, we used a surface level meter.

The utilization of a dewar necessitates the implementation of safety protocols. The first one arises from the fact that the volume ratio of gas and liquid is 700:1. If the dewar was not open to the return line, the inside pressure would rise to several atmospheres. The pressure gauges installed and the walls of the dewar are unable to withstand such forces and would consequently incur damage. In order to prevent this it is common to install safety gauges, which, in case of overpressure, would open and realease the gas out of the cryostat.

The experiments in the sub-kelvin temperature range meet with another complication. At the interface of the solid and liquid phases, occurs thermal Kapitza's resistance. This phenomenon occurs as a result of variations in the speed of sound among different states of medium. Kapitza's resistance is proportional to T^{-3}, which explains why it can be neglected at higher temperatures, even though it is a crucial restriction for reaching millikelvin temperatures.

2.1   Thermometry

Precise knowledge of temperature is essential part of cryogenic experiments. In low-temperature thermometry we use dependence of temperature dependence of various physical properties[1]. For example electrical resistance of the metallic thermometers shows almost a linear decrease with the temperatures. This holds true until the resistance reaches plato, it saturates. As a result, metal resistance thermometry cannot be used in very low temperatures. Due to that limit, we used PT-100 thermometers only during the precooling. In the lower temperatures, semiconductive RuO_2 thermometers are used, wherein resistance exponentially rises with the decreasing temperature. But for fine and precise temperature measurements of sub milikelvin temperatures, we use a SQUID-noise[2] thermometer MFFT-1 by Magnicon. Brownian motion of conduction electrons leads to the temperature-dependent fluctuation of electrical voltage. In the interval of frequencies, $(\nu + \Delta\nu)$, the mean square error of noise amplitude can be calculated by

$$\langle u^2 \rangle = 4kTR\Delta\nu. \tag{2.1}$$

where k is the Boltzmann constant and R is the resistance.

2.2   Dilution Refrigerator

In the previous Section, we discussed ways of measuring the temperatures, but we omitted how to ways to achieve sub-kelvin temperatures. One viable method for achieving this is by taking advantage of unique properties of a mixture of ^{3}He and ^{4}He. In the x-T phase diagram[3], see. Fig.2.1, there are three distinct

---

[1]These are secondary thermometers and they require calibration.
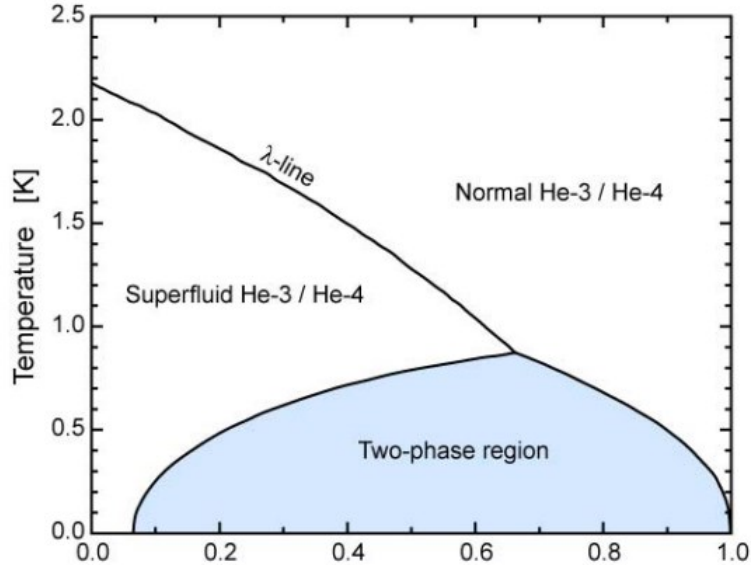[2]Superconducting QUantum Interference Device

Fig. 2.1: Phase diagram of the mixture of ^{3}He and ^{4}He. [29]

sections. While cooling the mixture in the normal phase, we can cross the λ line where the ^{4}He undergoes a superfluid transition. Another process arises if we cool the mixture down. In this case we arrive at phase separation region. Here the mixture separates into ^{4}He rich phase and ^{3}He rich phase. The density of these two phases is temperature dependent. These phases have different densities, from which follows that the less dense ^{3}He phase floats on the top. As we decrease the temperature, due to finite solubility, the diluted ^{3}He phase concentration does not reach zero. The cooling power of the dilution process origins in different enthalpy of diluted and concentrated phases and shows weaker temperature dependence than evaporation of cryoliquid.

We use commercial dilution refrigerator MNK-126 by Leiden Cryogenics, shown in Fig.2.2. A significant part of the dilution refrigerator is *mixing chamber*, where the transfer of ^{3}He is transferred from the concentrated to the diluted phase of the mixture. In the *still* ^{3}He is evaporated and returns to the circulation circuit. As a consequence of different evaporation temperatures, we can safely assume that the circulated substance is mainly composed of pure ^{3}He. During the whole circulation, the gas goes through various heat *exchangers*. Helium molecules in the circuit are transferred with a scroll and turbo-molecular pump.

Before releasing the helium mixture into the circuit, we used turbo-molecular pumps to drain the air from the gas handling system and the experimental cell. This is necessary because the internal components of a dilution refrigerator are made of thin capillaries, in which the non-helium gas could freeze and create a solid seal. This would prevent the helium mixture from the circuit and thus make the refrigerator unusable.

We have already established that vacuum purity is necessary for a properly working dilution refrigerator. To ensure this purity in the volume of the vacuum chamber, the coal trap is installed on one of the plates. The coal absorbs the impurities. After the experiment, the coal trap is heated by the AC voltage source,
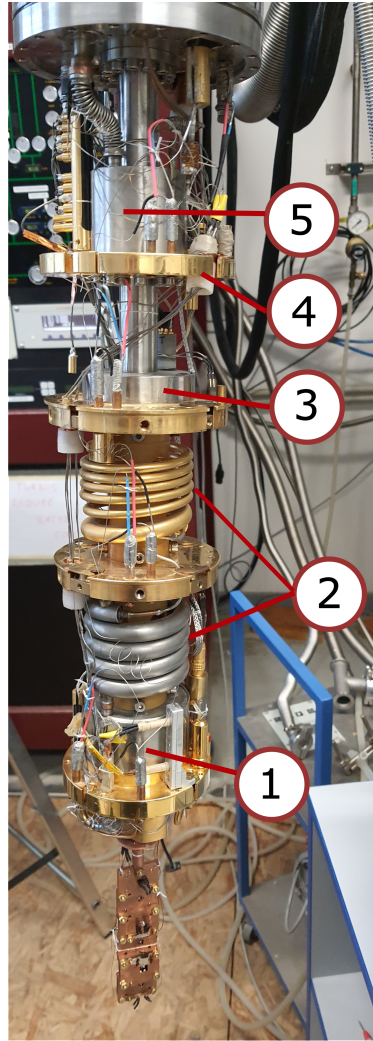
---

[3]x is the concentration of ^3He in the mixture

Fig. 2.2: Dilution refrigerator MNK-126. 1 - mixing chamber, 2 - heat exchangers, 3 - still, 4 - 1K plate, 5 - 1K pot.

leading to increased temperature and release of the trapped gases. Another way of trapping non-helium gas is to use cold traps. They are built of a tube placed in liquid nitrogen. When the non-helium gas travels through the cold trap, it lowers its temperature to a nitrogen level, condensates, and keeps them in the trap.

The last remaining inquiry is about temperature manipulation. Reaching higher temperatures is accomplished by introducing AC-powered heater to the system. After introducing small power to heater we can finely control the temperature in experimental cell.

Tab. 2.1: Electrical resistance of MEMS

WIRE	Mag. field range [mT]	Electrical Resistance [Ω]
G1L	31.5-81.9	4-6
G1R	31.5-81.9	4-6
G3R	31.5	0.1

2.3 MEMS devices

Our experiments use single-crystal, goal-post-shaped Microscopic Electrical Mechanical Oscillators (MEMS). These devices are placed in the homogenous magnetic field B, generated by a superconductive electromagnet provided with the cryostat, capable of reaching 9 T. Magnet is excited with driving AC electrical current I. This leads to the movement of the wires via Lorentz force

$$F = BLI \tag{2.2}$$

with L being leg spacing. Combination of driving current with measured induced Faraday voltage U regards the electrical response of MEMS with lorentzian character, described in Section 1.2.4. These properties can be recalculated to respective mechanical properties, i.e, Lorentz force defined in Eq. 2.2 and peak velocity of the microwire

$$v_{peak} = \frac{U}{BL} \tag{2.3}$$

All devices show gradual rise of electical resistance shown in Table. 2.1 This gradual change can be explained by the gradual rise of the aluminium film on the micro-chip. These devices are fabricated using optical lithography. Details of fabrications can be found in [30].

The experimental setup involved the utilization of three Microelectromechanical Systems (MEMS) devices, specifically a solitary G3R device and a pair of G1R and G1L wires, which were positioned on a single microchip. The motion of the wires was excited by the waveform generator Agilent 33220A with 10kΩ resistors and 20 dB attenuator. The response was measured by the Stanford Research Systems' phase-sensitive Lock-in SR830 and preamplified with voltage amplifier SR-560. Dimensions of the wires are provided in Table 2.2

The connections for double wire microchip is more complicated due to shared pin connection. For this microchip, the scheme of connections is shown in Figure 2.3.

Wires were placed in the experimental cell, shown in Figure 2.4. Wires G1L and G1R are denoted as 1,2, respectively, and 4 signifies the location of G3R.

Tab. 2.2: Dimensions of the MEMS used in the experiment l - length of the beam, h - leg height, t - beam thickness, w - width of the beam, m_{vac} is weight of MEMS in vacuum and resonance frequency in vacuum f_{vac}.

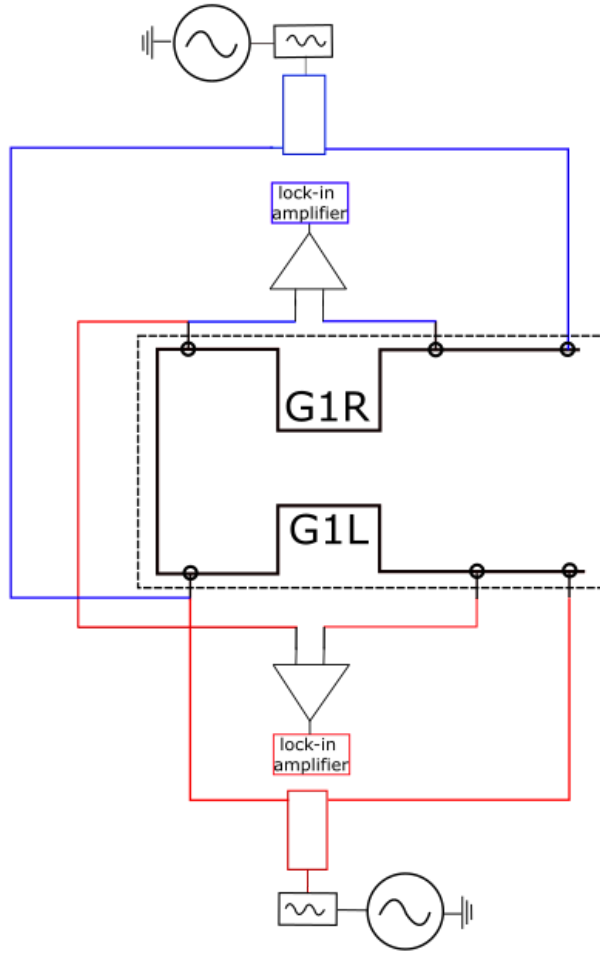| wire	l [mm]	h [mm]	t [μm]	w [μm]	$m_{vac} \times 10^{-10}$ [kg]	f_{vac} [Hz]
G1L	1	0.9	7	22	5.38	4911
G1R	1	1	7	22	5.20	5537
G3R	1	0.5	7	22	4.49	-

Fig. 2.3: Electrical scheme of a microchip with wires G1L and G1L.

Number 3 shows the location of the quartz tuning fork used for creating turbulence in the front of a double-wire microchip. Lastly, another quartz tuning fork was placed on the bottom of the channel insert, 5. After this fork was submerged in the fluid, its resonance frequency is shifted to lower frequencies. This is the reason why tuning fork is used for determining the state of filling the experimental chamber.
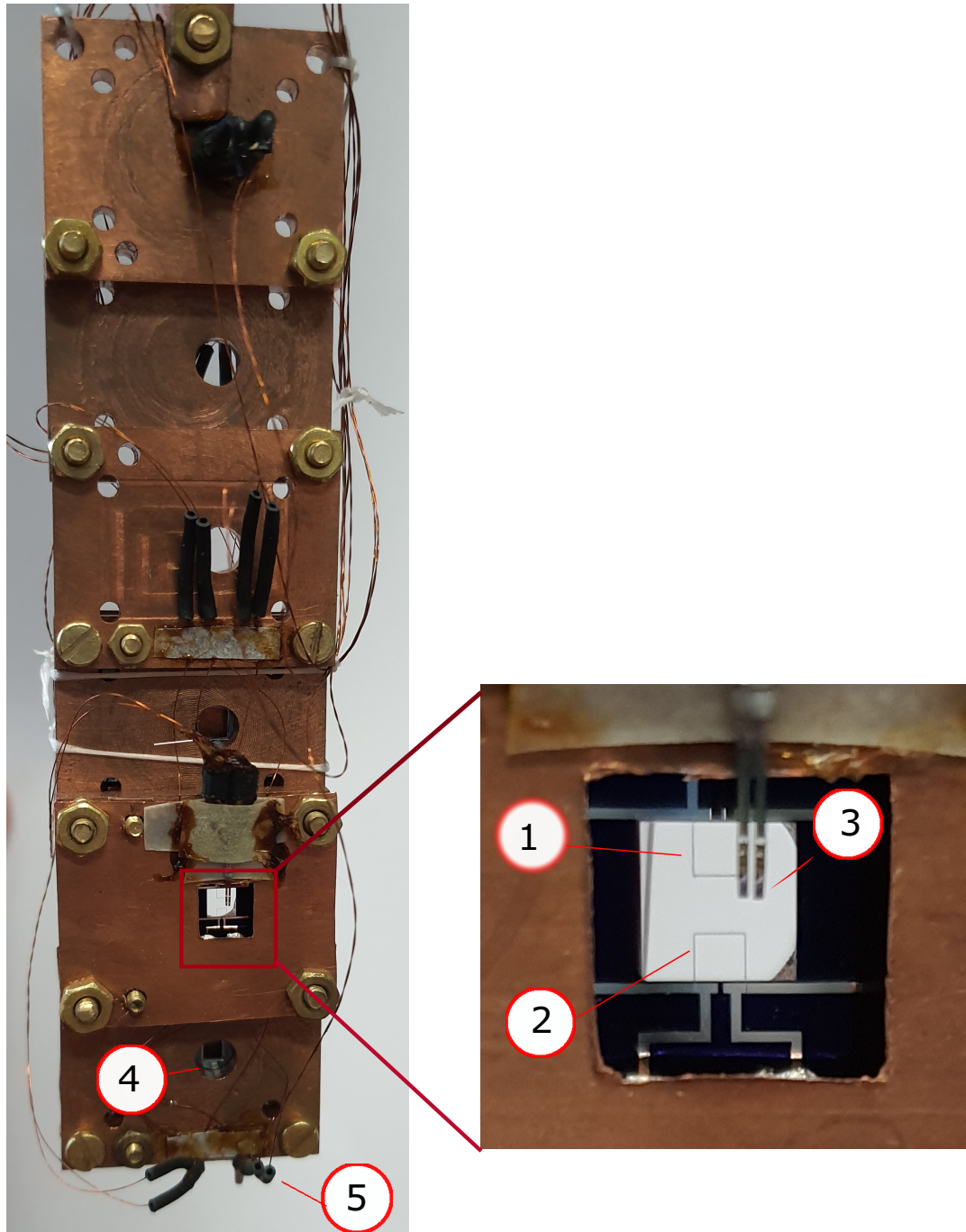
Fig. 2.4: Experimental setup on the insert of the chamber. 1 - G1L MEMS device, 2 - G1R MEMS device, 3 - tuning fork used for generating turbulence, 4 - G3R MEMS device, and 5 - tuning fork used while filling the chamber.

3. Results of measurement

Prior to the start of the experiment, we drained the air out of the system and thoroughly checked all the electrical connections.

After these necessary tests, we proceeded to the cooling of the experiment. Using a dilution refrigerator, we cooled the system down to T ≈ 20 mK. This was the lowest reached stable temperature, and we considered it the base temperature. All measurements were done in custom software programmed in LabVIEW environment.

In the first step we tried to find the resonant frequencies of oscillators in a vacuum in B = 13 mT. In the beginning, we could not find the resonance peak due to narrow FWHM and broad sweeping frequency range. Stated differently, the interval between neighboring frequencies was broader than the width of resonance peaks.We solved this issue by increasing the magnetic field to B = 63 mT, which led to a wider peak width and higher amplitudes. This change in the magnetic field does not significantly affect the resonant frequencies, so these new-found frequencies can be used to find the resonance peaks in the lower fields in the narrower frequency range. An alternative approach is to increase the driving voltage of the microwires. While increasing the drive, one must be careful, as this approach introduces a new heating source in the system. An example of one of the long-frequency sweeps for G1L wire is shown in Figure 3.1. In this Figure, we can see that instead of clear Lorentz resonance peaks, as in Figure.1.9, we measured the exponential decay of the system. This behavior can be explained by the fast
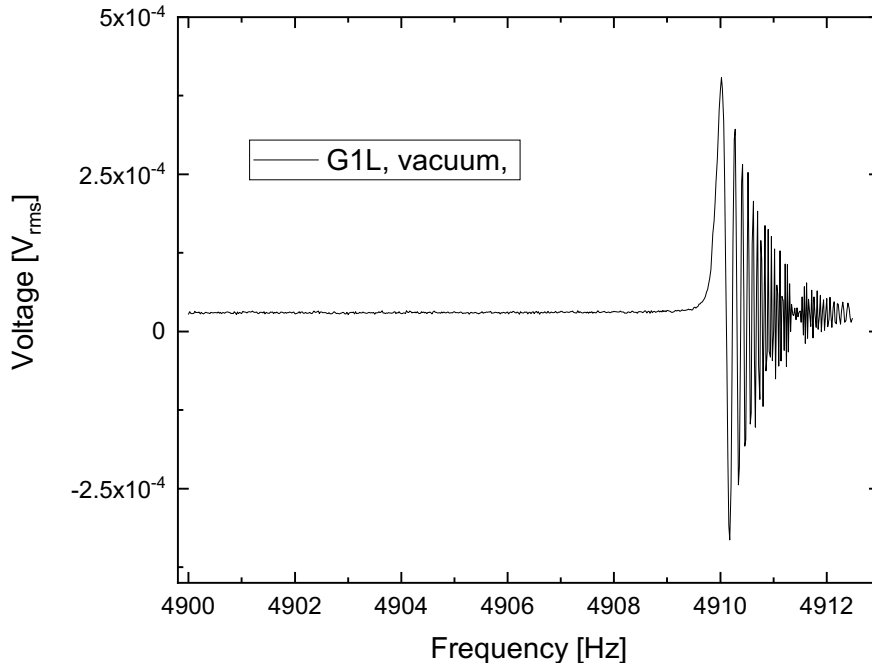
Fig. 3.1: Frequency sweep in long frequency range measured in a vacuum with G1L wire.

measurement in which the response of the oscillator did not have enough time to relax to a stable value. To ensure this will not happen, we set the measurement parameters to waiting for time $t_w = 80$ s and the Lock-in time constant to 10 s which should be better than minimal settling time $1/2\pi\Delta f$ where Δf represent FWHM. Table 3.1 shows the measured resonant frequencies for wire G1L, G1R, and G3R. The difference in resonant frequencies results from the different geomet-

Tab. 3.1: Measured resonant frequencies of MEMS in vacuum

	G1L	**G1R**	**G3R**
f_0 [Hz]	4909.97	5535.65	14868.19
Δf [Hz]	0.19	0.17	0.6

rical dimensions given in Table 3.1. This dependency can be seen in the similar resonant frequency of G1L and G1R wire, for which the only different dimension is the height of the legs. On the other hand, the G3R shows exceedingly different frequencies. The different resonance frequencies are necessary for simultaneous measurement on all three microwires, preventing the electrical cross-talk between induced electrical voltages. Measured resonant frequencies differ from frequencies previously found. This change will be discussed in Section 4.

After that, we made sequential measurements of the resonance curves with different driving voltages in the range of 0.1 V to 1 V. This measurement was repeated for five temperatures between 20 mK and 920 mK. Response of the oscillator above the temperature of 1000 mK was not measured because the oscillators transitioned from superconducting to normal state, given critical temperature of Aluminium. Measured data are shown in Figs. 3.3 - 3.8. At T = 500 mK we measured with voltages up to 6.95 V, see. Figure 3.5. Insert shows the resonance curve for the three lowest drives. These curves were measured from lower to higher frequencies and gradually transitioned from frequency-softening at low drives to frequency-hardening at high drives. All figures show the measured signal with subtracted electrical background and are plotted only for in-phase component of the signal. In the Figure 3.6 we show the out-of phase component of measured Faraday's voltage at T = 500 mK and B = 12.6 mT. This Figure shows highly non-linear behavior for drives 2.98 V and 6.95 V.

Figure 3.9 shows the wires' response in higher magnetic field B = 63 mT. It was measured from high to low frequencies. This signal shows the difference in amplitude compared to measurement in lower magnetic field. The change in frequency response might be caused by the geometrical non-linearities affecting the motion of the wire at lower driving voltages.

After vacuum measurements, we proceeded to filling of the experimental chamber. We used a quartz tuning fork to see if the liquid helium was in the chamber. We excited the resonance response from the tuning fork, with the resonance frequency 32712 Hz (black line in Figure 3.2). When the liquid helium reached the tuning fork, its motion was damped, which increased the FWHM of the resonance peak and shifted the resonance frequency to 32071 Hz. This frequency shift is shown in Figure 3.2.

The last measurement was done at T = 20 mK in the magnetic field B = 9.45 mK, for drives ranging from 0.43 V to 2.33 V and is shown in Figure 3.10. During the experiments, the supply of liquid He was limited, leading
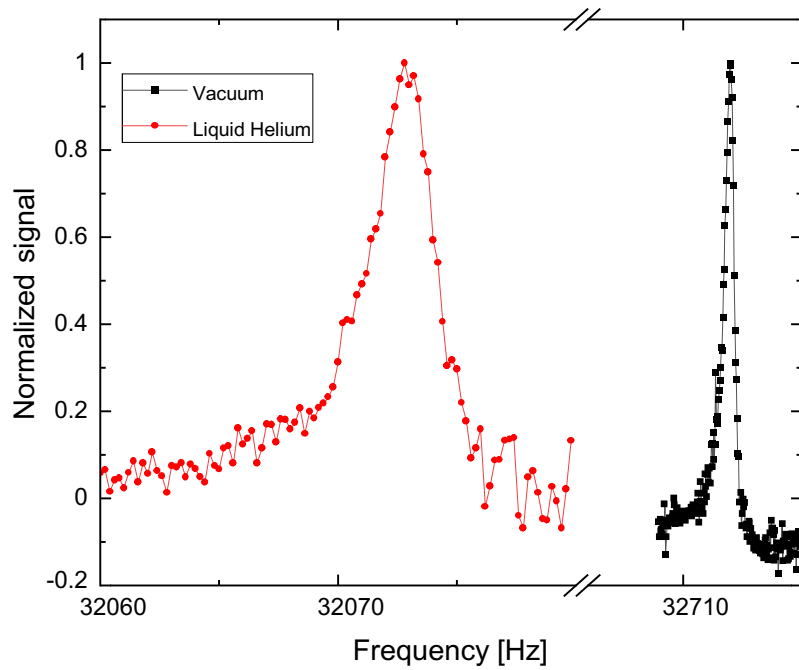
Fig. 3.2: Response of quartz tuning fork in vacuum (black) and in liquid helium (red) with clear resonance frequency shift and change in FWHM.

to the insufficient liquid inside the cryostat. As the liquid level dropped below the 1K pot of dilution refrigerator, some impurities probably got into a thin capillary connecting 1K pot and the liquid helium bath. This resulted in its blockage, and we were forced to stop the experiment. In the following Chapter, a discussion of the results will follow.
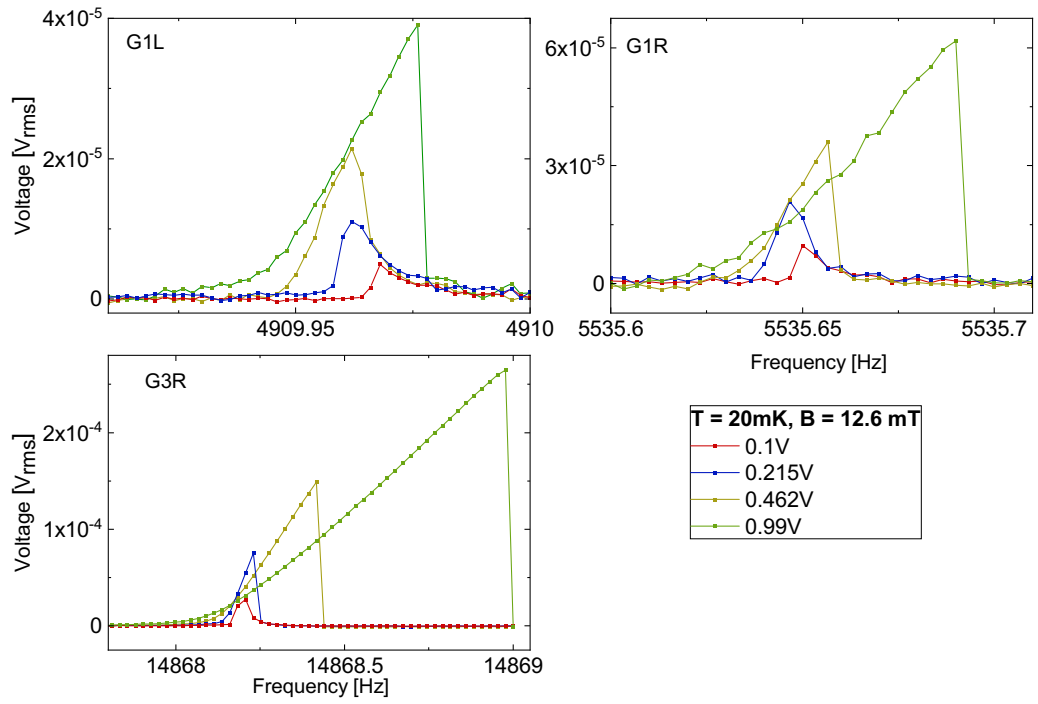
Fig. 3.3: Low to high frequency sweep of G1L (upper left), G1R (upper right) and G3R (lower left) at B = 12.6mT and T = 20 mK in vacuum.
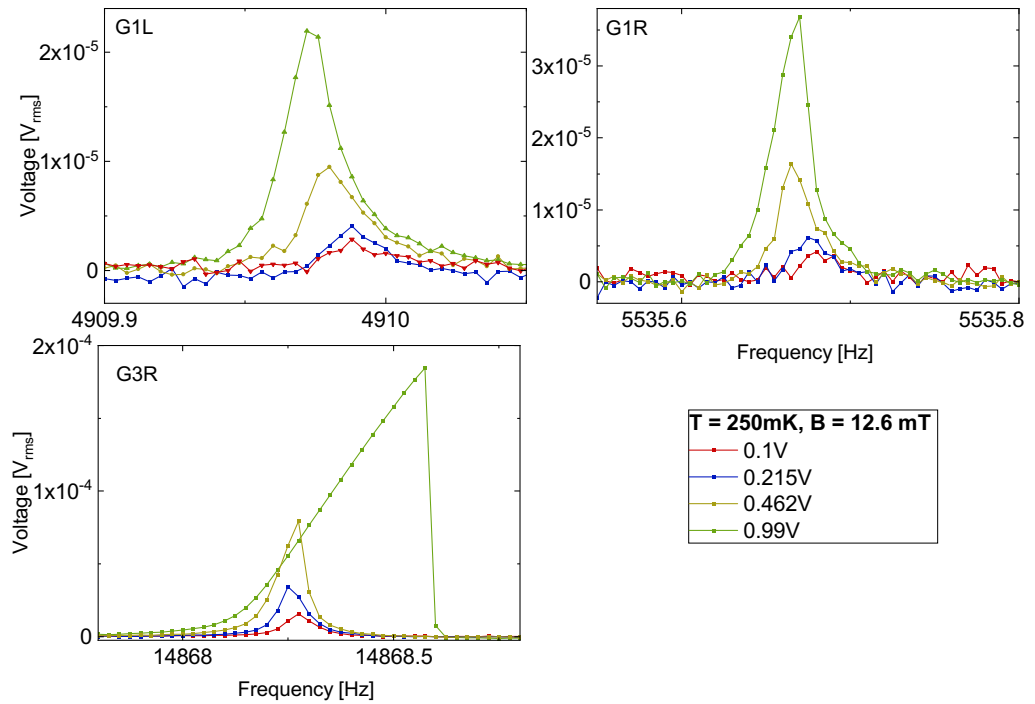
Fig. 3.4: Low to high frequency sweep of G1L (upper left), G1R (upper right) and G3R (lower left) at B = 12.6mT and T = 250 mK in vacuum.
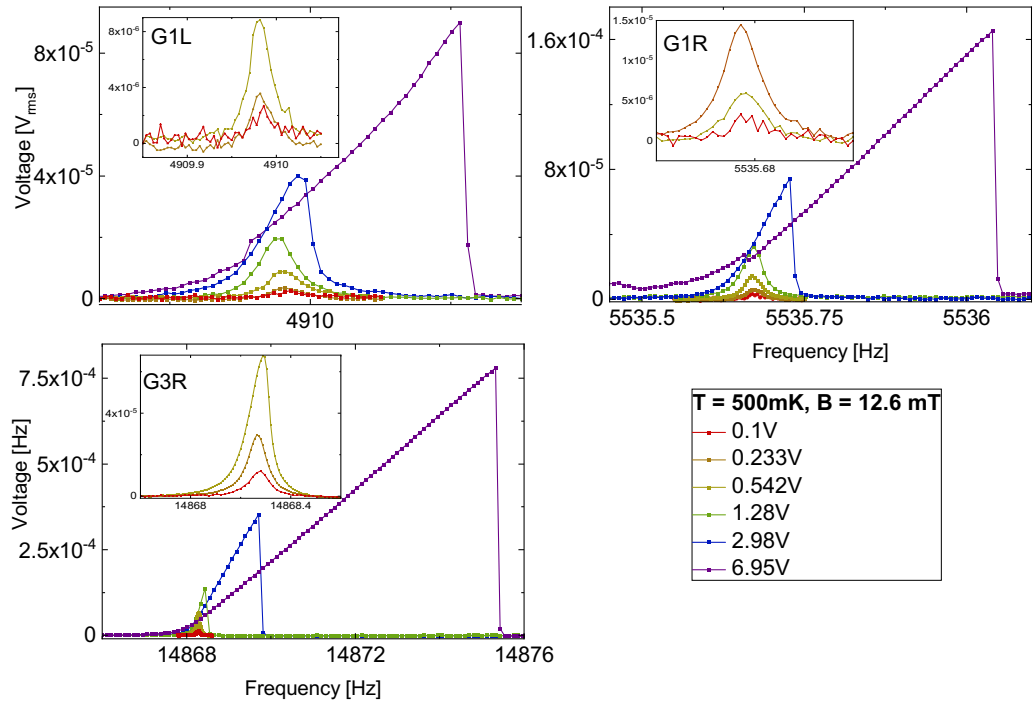
Fig. 3.5: Low to high frequency sweep of G1L (upper left), G1R (upper right) and G3R (lower left) at B = 12.6mT and T = 500 mK in vacuum.
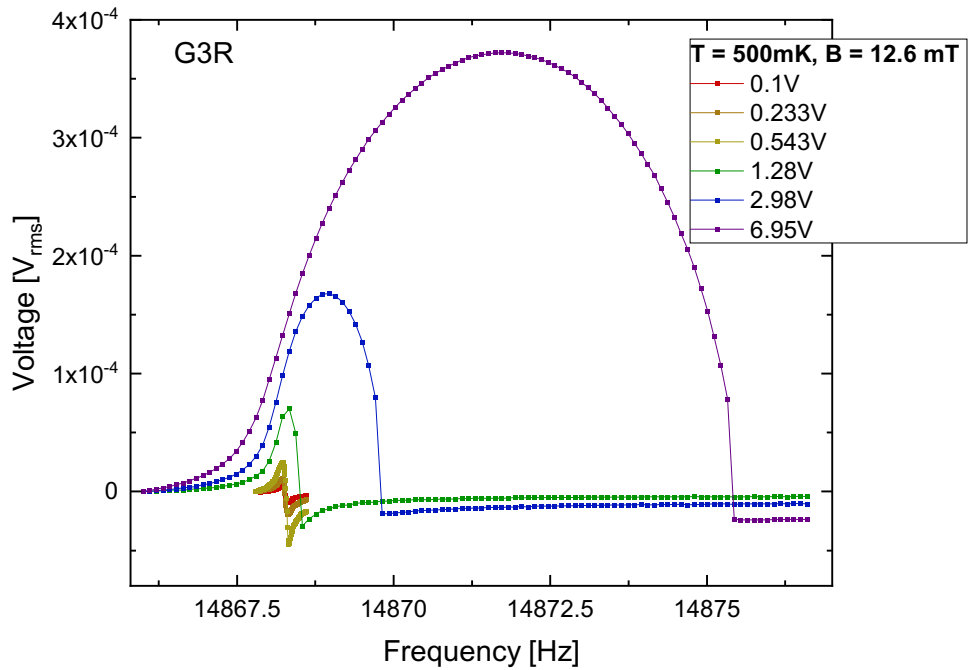
Fig. 3.6: Out of phase component of the induced voltage on G3R wired measured at T = 500 mK and B = 12.6 mT. The signals with drives 2.98 V and 6.95 V shows high non-linear behavior.
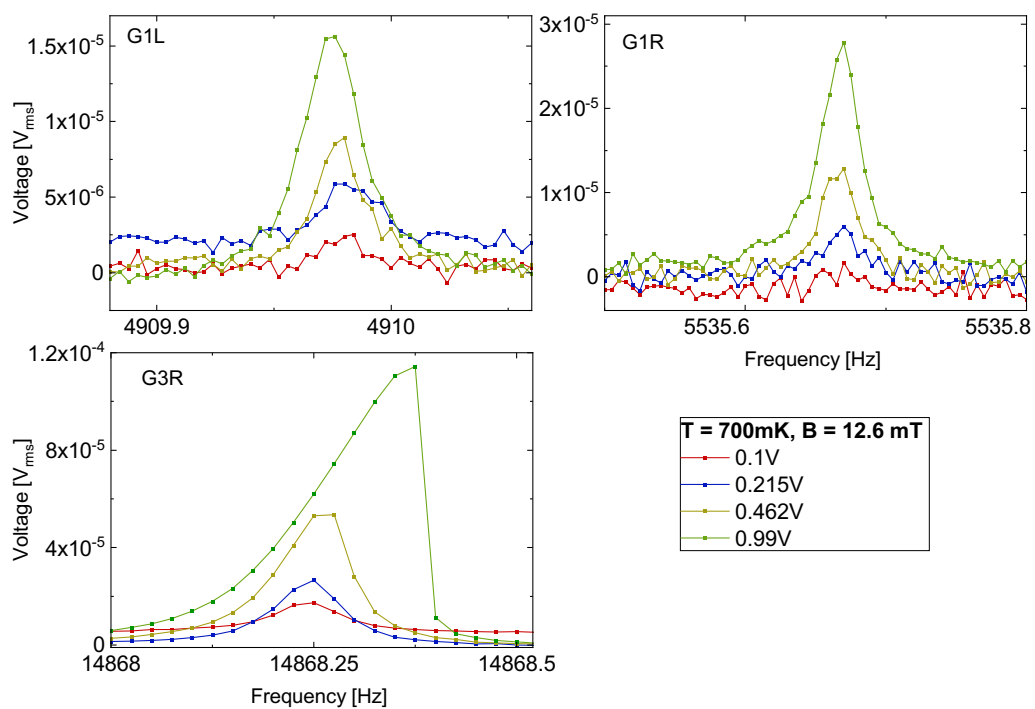
Fig. 3.7: Low to high frequency sweep of G1L (upper left), G1R (upper right) and G3R (lower left) at B = 12.6mT and T = 700 mK in vacuum.
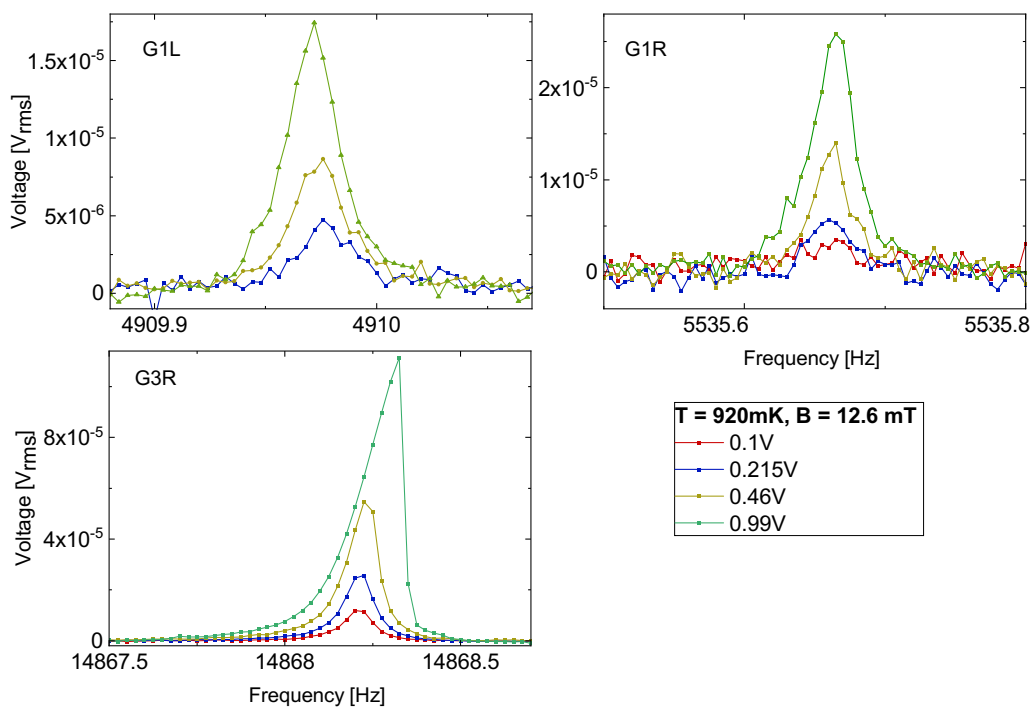
Fig. 3.8: Low to high frequency sweep of G1L (upper left), G1R (upper right) and G3R (lower left) at B = 12.6mT and T = 920 mK in vacuum.
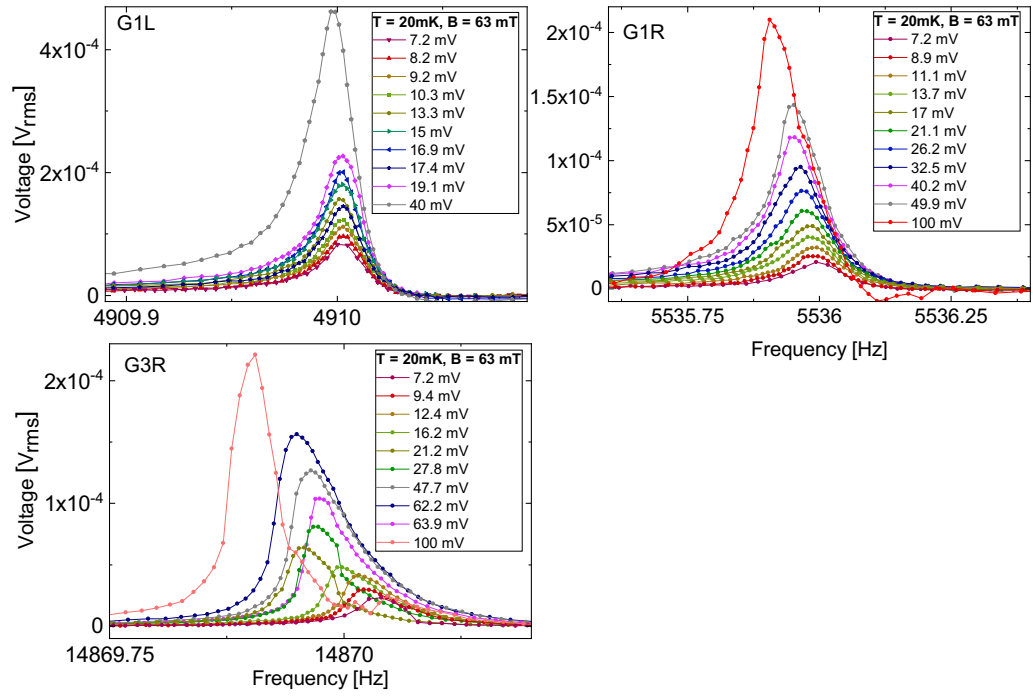
Fig. 3.9: High to low frequency sweep of G1L (upper left), G1R (upper right) and G3R (lower left) at B = 63mT and T = 20 mK
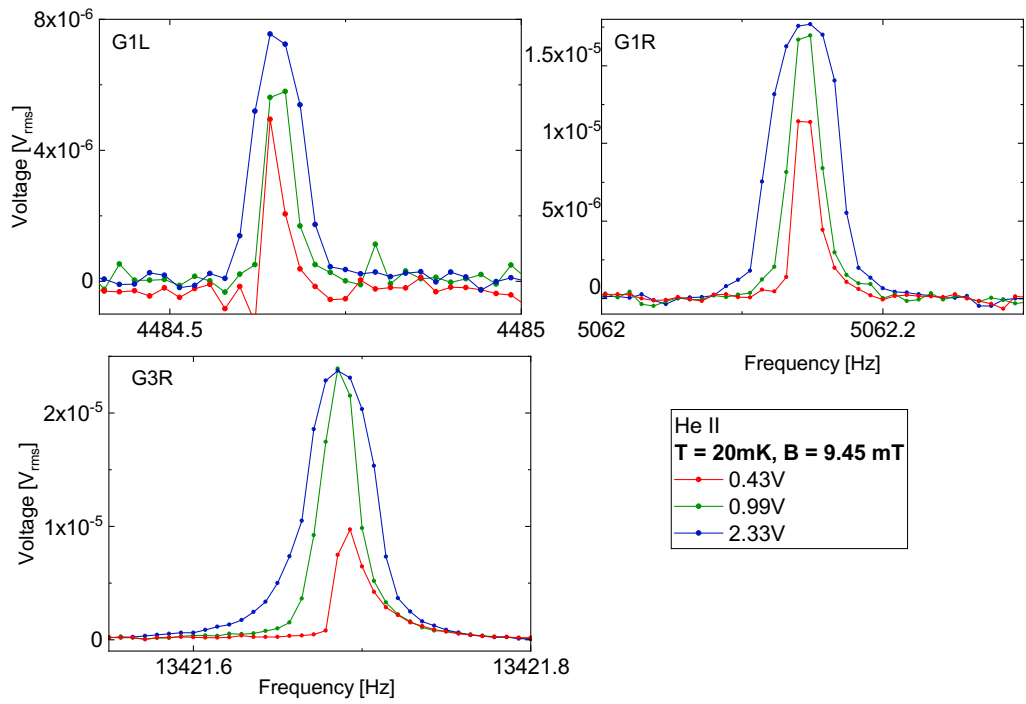
Fig. 3.10: Low to high frequency sweep of G1L (upper left), G1R (upper right) and G3R (lower left) at B = 12.6mT and T = 20 mK in He II.

4. Discussion

First, we will analyse results measured with 100x amplification in vacuum, see Figures 3.3 - 3.8. The amplitude of the resonance peak scales with the driving voltage, according to Eqs. 2.2 and 2.3. The driving current was determined using Ohm's law. For voltages up to 0.462 V, the peaks are Lorentzian. In stark contrast to that highly driven peaks show nonlinear behavior. Amongst the wires G3R showed the most non-linear behaviour. This can be explained by its shortest length. This leads to higher mechanical tension with the same displacement. Measurement at higher magnetic field B = 63 mT, provided in Figure 3.9, shows the same behaviour as the lower fields, only with higher amplitudes. Overall signals received from low drives show a frequency-softening; the response flips to hardening for higher drives. This may be caused by the geometrical nonlinearities in addition to changes in nonlinear stresses inside the thin metallic layer. Similar softening-hardening behavior was seen in [31]. In forthcoming measurements, our intention is to replicate the experiment while adjusting the sweeping direction in accordance with the specific type of non-linearity. For frequency-hardening, it is adequate to use low to high-frequency sweep and vice versa for frequency-softening. Frequency sweep in the opposite direction can show hysteresis more discussed in [32]. An alternative approach to characterizing resonance behavior
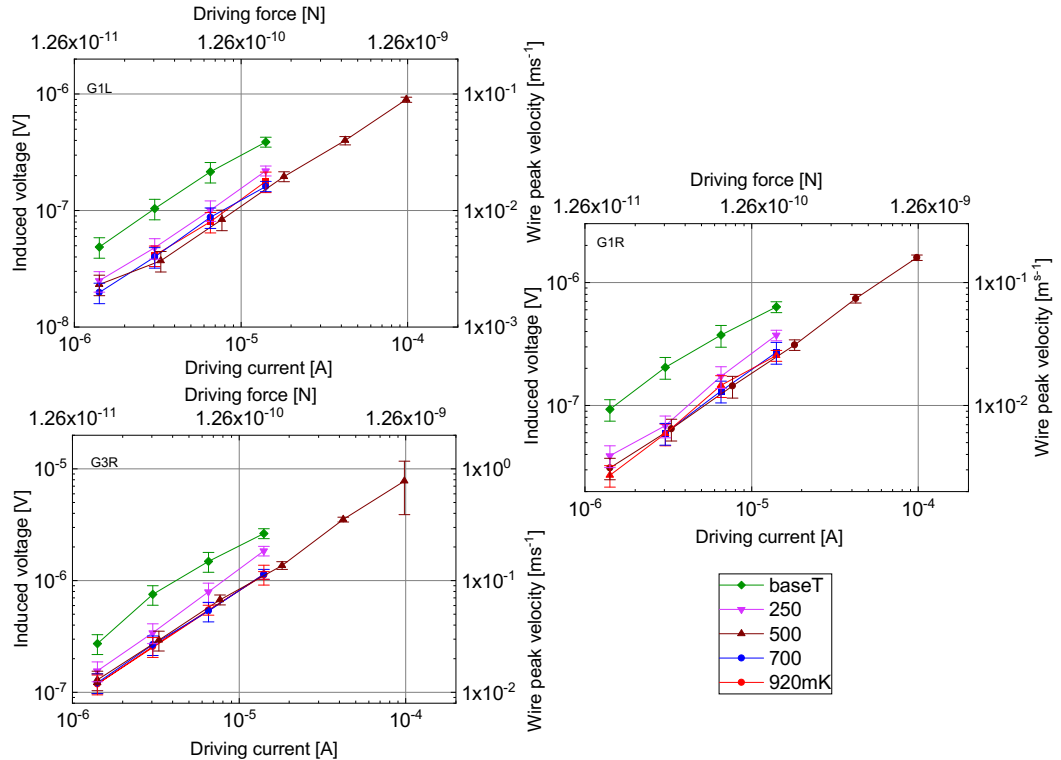
Fig. 4.1: Log-log dependency of electrical properties (driving current and induced voltage) and their related mechanical properties (driving force and wire peak velocity) plotted for all measured temperatures and drives in the magnetic field B = 12.6 mT and were measured with 100x amplification. All MEMS shows the same linear behaviour with the same slope.
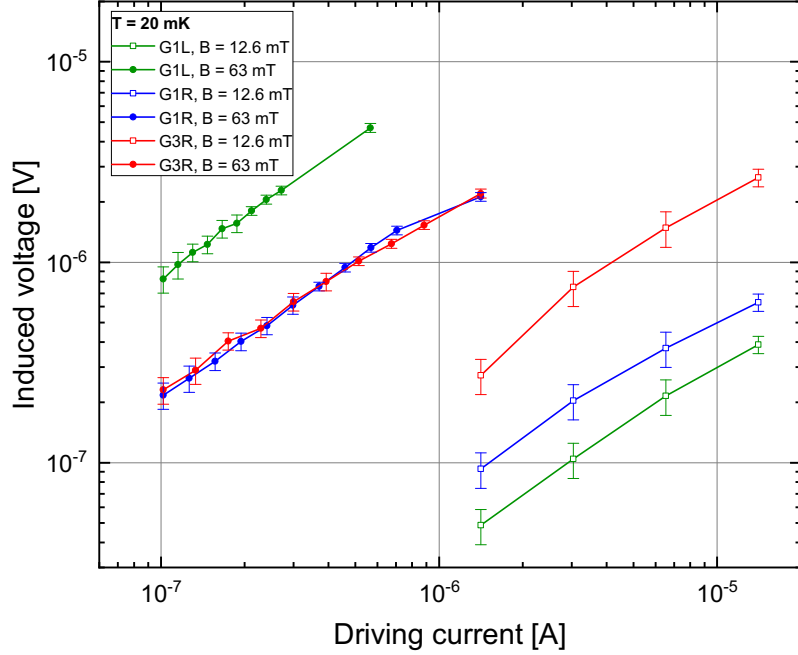
Fig. 4.2: Log-log comparison of electrical properties (driving current and induced voltage) measured at magnetic field B = 12.6 mT and B = 63 mT. All MEMS shows the same linear behaviour with the same slope and differs in their amplitudes.

is using the quality factor defined as

$$Q = \frac{f_0}{\Delta f} \tag{4.1}$$

where f_0 is the resonance frequency of the peak and the Δf is FWHM.
In the next Section, we will discuss the width of the resonance peaks. This quantity is correlated with the inverse of the quality factor and thus it gives us the quantitatively the same information about the system as the Q-factor.

4.1 Measurement in vacuum

The first step in describing oscillating devices is to calculate the relationship between electrical properties (driving current and induced voltage) and the corresponding mechanical properties (driving force and wire peak velocity). These properties were calculated using formulae given in Section 2.3. Unless otherwise mentioned, all values are given as RMS (*Root Mean Squared*). Interrelationship between mechanical and electrical properties is shown in Figure 4.1. Induced voltages are plotted as amplitudes using $U_{amp} = U_{rms}/\sqrt{2}$. The driving current exhibits a linear correlation with the induced voltage, as anticipated, owing to the sole presence of linear dissipation within the material.

The same analysis was repeated for measurement in the higher magnetic field at T = 20 mK and is shown in Figure 4.2. This graph shows the difference between
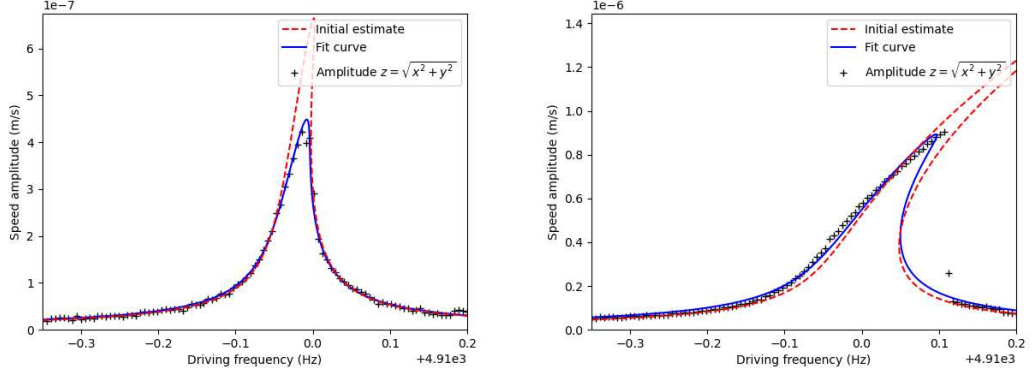
Fig. 4.3: Complex amplitude fit of experimental data for G1L wire driven by V = 500mK for drives U = 2.98 V (left) and U = 7 V (right) with clearly seen frequency hardening.

the same MEMS measured in low and high magnetic fields. Even though datasets are not measured at the same driving currents, we assume the trend extends even to higher drives. As expected, both lines show almost linear behavior with the same slope, and results differ only in the amplitude of induced voltages.

Analysis was conducted by fitting the measured data. We used custom made Python software developed by Marek Talíř and discussed in [28]. Software fits only the complex amplitude z = Re(x) + Im(x) and does self-correction for phase and background. While fitting vacuum data, we only considered linear damping, described by γ_1 and the higher order damping parameters were fixed to constant zero. We used the weight function in the shape of a Gauss curve to compensate for a low number of measured points on the peak.

Example fit of the G1L dataset at T = 500 mK for driving voltages 2.98 V and 7 V is provided in Figure 4.3. The red curve shows the initial guess of the fitted curve and the blue curve shows final fitted curve. Even though the initial guess does not align well with the measured data, the final curve fits well. The evolution of resonance peak width Δf with different drives is shown in Figure 4.4. The fit of resonance peak at V = 7 V_{rms} did not converge so we removed it from this analysis. Resonance peak at T = 20 mK (red points) shows smallest width and its rise might be caused by geometrical distortions of the device or by entrapment of magnetic flux quanta in the device. Difference between T = 20 mK and other temperatures can be explained by transition to resistive state which introduce additional dissipation mechanism. In the future, we will focus our attention on measurement with finer driving currents at different temperatures.

To evaluate validity of the fitting procedure we can compare obtained results with the quantitive analysis. From measured data we see that width of the resonance curve is: for G1L and G1R in 12 mT fields only 10 Hz, but for fields they broaden to 26 mT and more. For G3R we can see that in lowest field its width is 40 Hz. G3R wire was not measured at higher fields. These quantitatively obtained data lies are in agreement with qualitative fitting procedure. Broadening of the resonance peak implies presence of new dissipative force, MEMS transition to resistive state.

Magnetic field place crucial part in our experiments. Mechanical force exciting

the oscillations of MEMS is function of magnetic field. Similarly detected velocity of oscillator is deeply affected by the magnetic field. Until this point we have fully omitted effect of external magnetic field and we will adress its' effect in following Section.

4.1.1   Response of MEMS in different magnetic fields

In this Section we will discuss response of MEMS in different magnetic fields. In the upcoming analysis, we will use data measured in our experiment, see Figure 3.5 and in an experiment conducted by Šimon Midlik, who measured resonant response of the same G1L and G1R wires at different magnetic fields B. Both measurements were conducted at T = 20 mK in magnetic fields 12.6 mT, 37.8 mT, 252 mT, 504 mT. Single dataset was obtained in lowest field B = 12.6 mT and higher temperature of 500 mK.

To demonstrate effect of magnetic field, in Figures 4.5 and 4.6, we present the maximum displacement of MEMS as function of the lorentz driving force. Peak displacement x, was determined from the peak velocity and resonance frequency f_0 of device as

$$x_{amp} = \frac{v_{amp}}{2\pi f_0}, \tag{4.2}$$
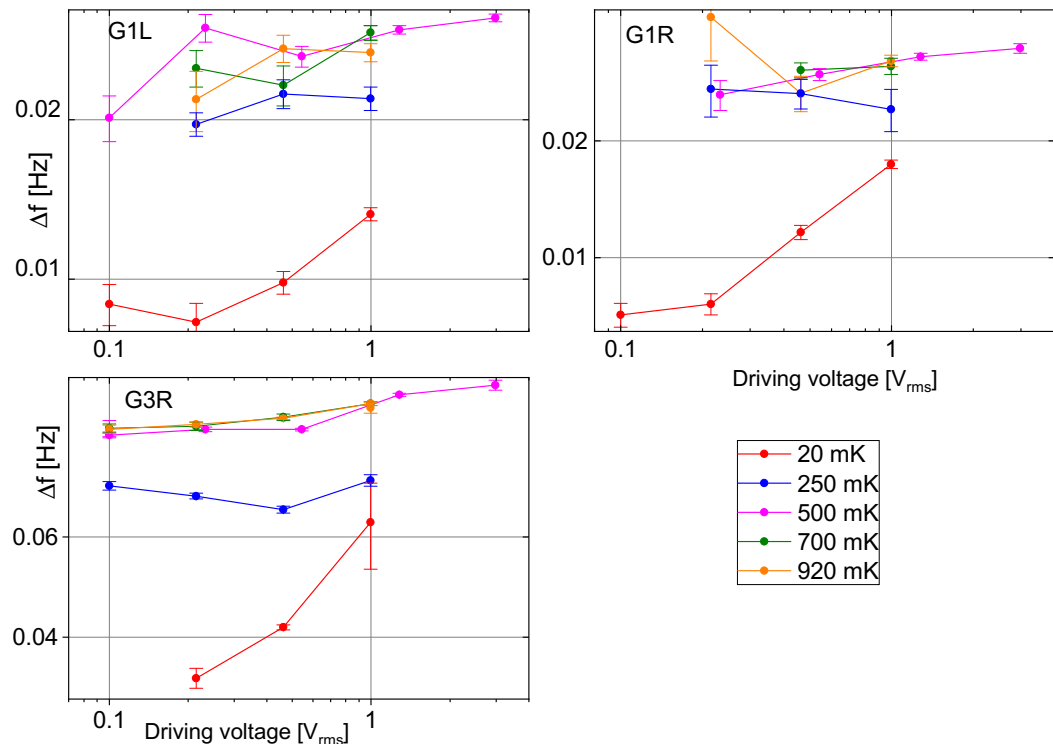
Fig. 4.4: Evolution of the resonance peak width Δf received from a fit of experimental results for all wires and all temperatures in vacuum. For most points, the dependence is constant with discrepancy for driving voltage V = 7 V in T = 500 mK. Due to a inefficient number of points at the peak, the fit of the resonance peak at V = 7 V did not converge with the required accuracy and it was removed from this discussion. Devices shows significant rise of damping in the temperature higher 20 mK which is explained by transition to resistive state.
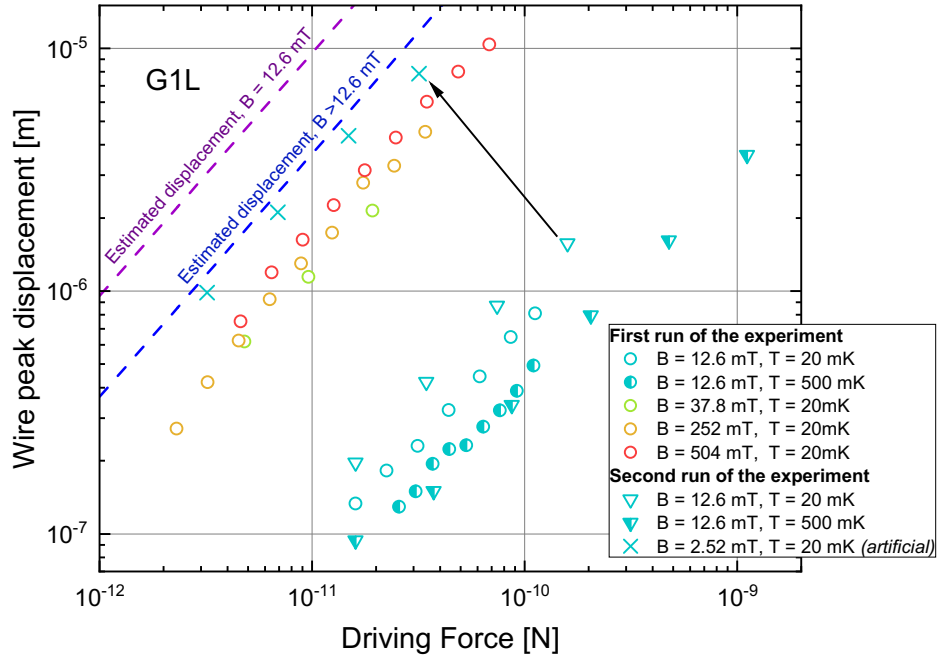
Fig. 4.5: Wire peak displacement as a function of driving current for G1L wire in vacuum. Lower displacement measured at B = 12 mT (cyan) is caused by fero-magnetic properties of radiation shield in apparatus. This effect is demonstrated by artificially changing the magnetic field (cyan crosses), see text for details.
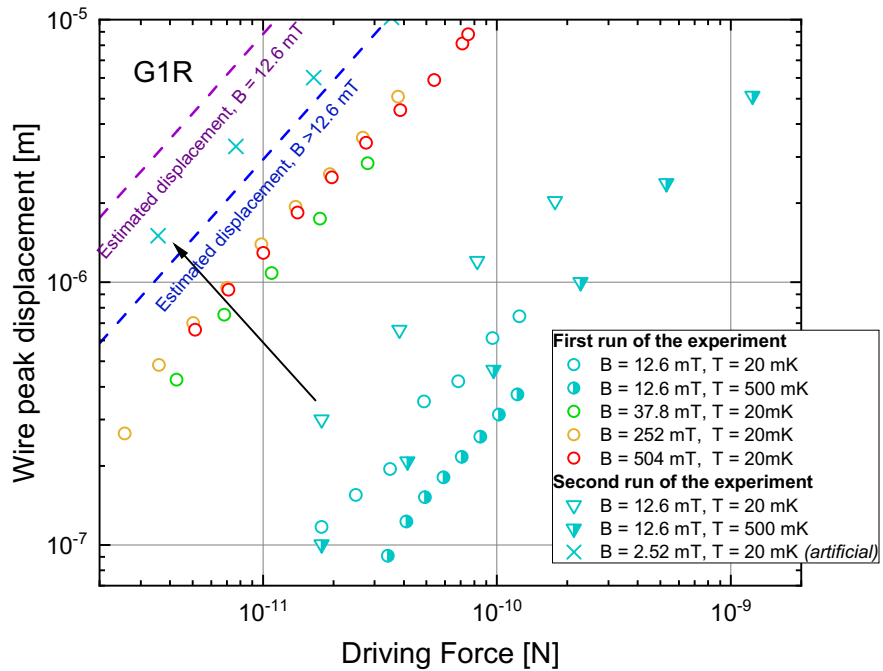
Fig. 4.6: Wire peak displacement as a function of driving current for G1R wire in vacuum. Lower displacement measured at B = 12 mT (cyan) is caused by fero-magnetic properties of radiation shield in apparatus. This effect is demonstrated by artificially changing the magnetic field (cyan crosses), see text for details.

and the estimated amplitude was obtained from Q-factors as

$$\frac{F}{x_{amp}} = \gamma_1 \omega_0 m_{eff} = 4\pi^2 m_{eff} \Delta f f_0. \tag{4.3}$$

As a consequence of different resonance linewidths for datasets in field 12.6 mT and in higher fields we show two lines depicting estimated amplitude, *purple* for fields 12.6 mT and *blue* for other fields. With the exception of responses from magnetic field B = 12.6 mT all data lies on single line. Origin of this difference lies in radiation shield in our apparatus. This shield is made out of stainless steel 304 which, although marketed as "non-magnetic steel", shows fascinating ferromagnetic properties. Childress et. al. [33] showed, that the mass magnetization of stainless steel 304 saturates at 130 emu/g[1] which corresponds to saturation field of $B_s = 16$ mT. From that follows that magnetic field of 12 mT is not sufficient enough to saturate the magnetization in steel shield and the wire thus experiences lower effective field. This effect is significant as both driving force and wire displacement is dependent on magnetic field. To demonstrate this effect we have artificially lowered the magnetic field in our calculation to a one fifth of the nominal value. Resulting data (cyan cros in 4.5 and 4.6) lies right with the other data points. Data measured for fields higher than 12.6 mT does not lie on the expected value (blue dashed line). This difference cannot be explained by losses in electrical circuit, thus we believe that it is caused by unknown electrical losses on the microchips. In the following discussion we will provide real magnetic field in our experiment. The corrections required for G1L/G1R wires and the G3R wire exhibit notable differences. While a similar field on G1L and G1R can be attributed to nearly identical spatial locations, the G3R wire is subjected to a higher magnetic field intensity. This disparity arises from the presence of sharp edges surrounding the lower region of the vacuum shield, where the G3R wire is placed. Consequently, the magnetic field lines penetrate the interior of the shield.

Effect of temperature can be seen in the same figure by half-full symbols. In the same Figure we show the results obtained from measurement at higher temperature. Displacement at 500 mK is smaller than at 20 mK. That can be explained by the transition of device to resistive state, see Section 4.1. Resistive state comes with higher dissipation rate which lowers the Q-factor of resonance peak. This leads to lower maximum displacement of the device.

4.2 Measurement in He II

In this Section, we will be discussing the response of MEMS in He II; see Figure 3.10. The difference in measured data is striking. The resonance peak is broader for the highest driving current, V = 2.33 V, than for the lower drives. This may be caused by the interaction of MEMS devices with quantized vortices. This type of response corresponds to turbulence generation from remnant vortices as observed by other oscillating devices - oscillating wires [24] or vibrating forks [25]. In order to prove this turbulence hypothesis we will again draw the dual plot of driving current to induced voltage and mechanical driving force to wire peak velocity; see Figure 4.7. Here we can see that, unlike the vacuum measurement,

---

[1]Figure 2 in [33]

Figure 4.1 the induced voltage is not linear with the driving current but it is flattened. In other words, the motion of the MEMS is affected by the flow of He II in its surroundings. This again points to the possibility of turbulent flow in the experimental channel. As a consequence of insufficient number of points on the resonance peak this measurements suffers from high inaccuracy of measured amplitude of induced voltages. This mainly affects measurements conducted with drives 0.43 and 2.33 V

Tab. 4.1: Critical voltages and velocities of MEMS in He II.

wire	V_{crit}[V]	v_{crit} [mm/s]
G1L	0.08	6
G1R	0.013	20
G3R	0.1	26

The subsequent step in the analysis involves fitting nonlinear peaks with the same custom-made Python software as in Section 4.1. In this case we considered linear and quadratic damping, described by quadratic damping coefficient $\gamma 2$. We chose a slightly different fitting model because the resulting fitted curves were significantly more stable. In Table 4.2 we present the result of a data fitting procedure applied to measurements conducted in the He II. In contrast with the vacuum measurement, Figure 4.4), the resonance peaks are more damped. This behaviour again leads to the conclusion that the flow around the MEMS is for driving voltages 0.99 and 2.33 V already turbulent. Motion of MEMS in He II generates quantized vortices similar to classical case, see Section 1.1.1. Eddies reconnect and lead to full-on quantum turbulence. They interact with MEMS by receiving their energy. This effect explains increase in FWHM of resonance peaks for driving currents 0.99 V and 2.33 V. In the future, we will replicate the experiment at more driving voltages. This will allow us to see the transition point
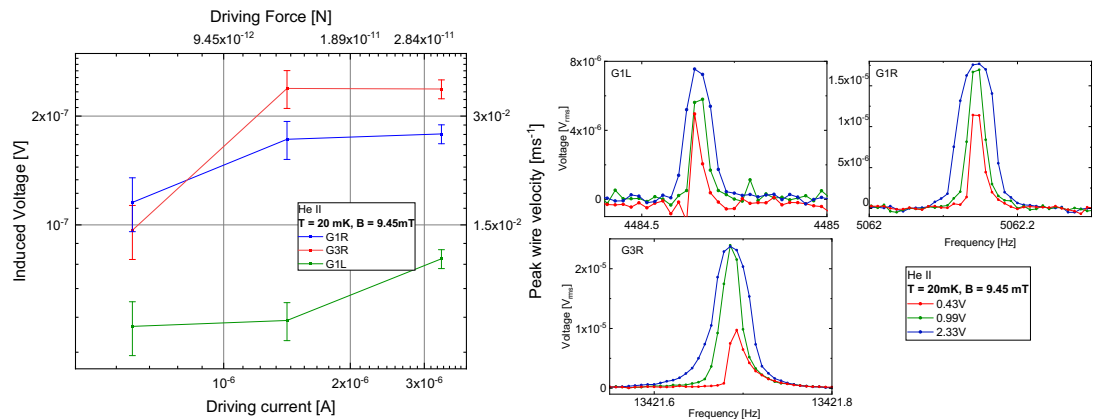
Fig. 4.7: Left: Log-log dependency of electrical properties (driving current and induced voltage) and their related mechanical properties (driving force and wire peak velocity) plotted for all driving voltages at the temperature T = 20 mK in B = 12.6 mT in He II. G1R and G3R MEMS shows flattening of the curve for driving current higher than I = 1.4 μA. This implies generations of quantised vortices by MEMS the experimental channel. Right: Measured data in He II at T = 20 mK and B = 9.45 mT.
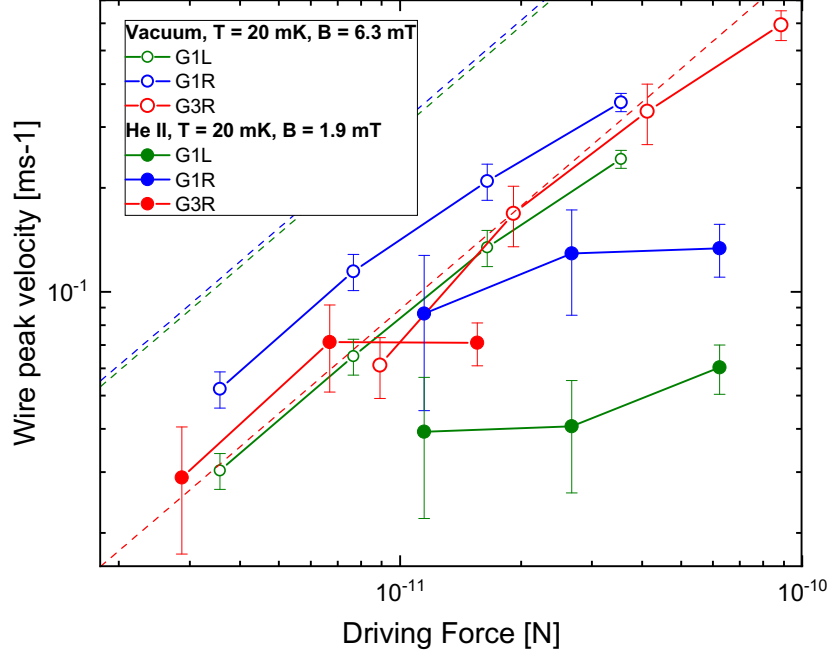
Fig. 4.8: Comparison of peak velocity as a function of driving voltage for measurement in vacuum (full symbols) and in He II (empty symbols) at the same temperature T = 20 mK. Peaks measured in helium show high non-linear damping; thus, MEMS in the experimental channel already generate quantised vortices. Dashed line represent estimated velocity of MEMS.

to turbulence, as the force-velocity response will change in character from linear to quadratic or a higher power law. This behavior lets us estimate critical velocities of MEMS and afterwards (using Equation 2.3) determine critical velocities. These results are shown in Table 4.1. Due to long relaxation times one frequency sweep took 2 hours and 42 minutes which with addition to blockage of the capillary lead to insufficient amount of driving voltages.

In Figure 4.8, we show the difference in peak velocity as a function of driving voltage for measurement in vacuum (full symbols) and in He II (empty symbols) at the same temperature T = 20 mK. With dashed line we present the estimated velocity of MEMS calculated from Equation 4.2. In fully laminar flow, its velocity

Tab. 4.2: Fit parameters of measurement in He II depicting the evolution of the linear damping coefficient γ_1, quadratic damping coefficient γ_2, and coefficients α_1, α_3 from Duffing's equation 1.32 of experimental results for all wires in T = 20 mK and B = 9.45 mK in He II. For increasing drive, the γ_2 rises rapidly, implying that the quantised vortices damp the motion of MEMS in a nonlinear fashion.

wire	V_{rms} [V]	f_0 [Hz]	$a_1 \times 10^8$ [N kg^{-1} s^{-2}]	$a_3 \times 10^{27}$ [m^{-2} s^{-2}]	γ_1 [s^{-1}]	$\gamma_2 \times 10^5$ [kg m^{-2}]
G1L	0.1	4484.6	0.79	1.80	0.03	5.37
G1L	0.233	4484.6	0.79	-2.11	6.45 $\times 10^{-9}$	16.4
G1R	0.043	5062.1	1.01	-33	0.02	0
G1R	0.1	5062.1	1.01	-65	0.004	1.21
G1R	0.233	5062.1	1.01	-33	1.1 $\times 10^{-8}$	4.27
G3R	0.043	13421.69	7.11	-0.24	0.014	0
G3R	0.1	13421.69	7.01	-1.41	2 $\times 10^{-7}$	0.92
G3R	0.233	13421.67	7.01	-1.19	1.7 $\times 10^{-7}$	2.2

should connect to vacuum data. In our case experiments does not perfectly align. This can be explained if the flow around our devices is already turbulent. To confirm that we can used known relationship between resonance frequency f_0, quantum of circulation κ and critical velocity, where flow transitions to turbulent state

$$v_{crit} = \sqrt{2\pi\beta\kappa f_0}. \tag{4.4}$$

Value of constant β can be determined as 0.53. To calculate that we determined critical velocity of G3R wire as intersection of vacuum and helium curve in Fig. 4.8. Critical velocities for wires are 0.07 ms^{-1} for G3R wire, and 0.04 ms^{-1} for other wires. Thus we can conclude that all wires were measured already in turbulent flow. Hypothesis of quantum turbulence also supports the increase of resonance line width of MEMS from 10 to 25 Hz for G1L and G1R wire. Quantum turblunce had to be generated by MEMS themselves. In this analysis we have assumed same correction with respect to magnetic shielding. In the future we will closely study properties of MEMS in low magnetic field, which can lead to removing this strong assumption.

4.2.1   Hydrodynamic description of MEMS in He II

All results discussed above point to the MEMS's ability to locally probe quantum turbulence created by themselves, similarly to slightly larger semicircular wires in thermal counterflow, see Attachment A.1.

Another useful analysis lies in converting frequency shifts of resonance frequency to changes in effective mass. From the resonance frequency in vacuum f$_0$ and resonance frequency in He II f we can determine Δm_{eff} using Equation

$$\Delta m_{eff} = m\left(\frac{f_0^2}{f^2} - 1\right) \tag{4.5}$$

Mass of MEMS m is provided in Table 2.2. The final results are shown in Tab. 4.3. All MEMS have the same basic mode shape of resonance profile and the ratio of densities of helium and silicon is constant. From that follows the ratio of Δm_{eff} and m should also be constant. The effective hydrodynamic mass of goalpost-shaped MEMS can be determined as $\rho_{Si}(V_{BEAM} + 0.5V_L)$ where ρ_{Si} is the density of silicon, V_{BEAM} is the volume of beam and factor 0.5 before the volume of legs V_L takes in an account number of legs (factor 2) and the resonance profile of leg (factor 1/4). Assuming that the relevant volume for flow past the wire is comparable to the volume of the wire itself, we can estimate the flow enhancement factor ϵ using the equation

$$\epsilon = \frac{\rho_{Si}}{\rho_{He}}\frac{\Delta m_{eff}}{m_{vac}} \tag{4.6}$$

Flow enhancement factor for G1L and G1R is 3.7 and 3.65, respectively and for G3R is 4.23; all of these are constant with 10% margin of error. Because of $\epsilon > 1$, we can conclude that flow around the MEMS is accelerated, which agrees with the classical description of flow around the bodies with sharp corners; for more info, see [13].

Another comparison can be made with the numerical results from [34]. They calculated hydrodynamic function with respect to aspect ratio of an oscillating
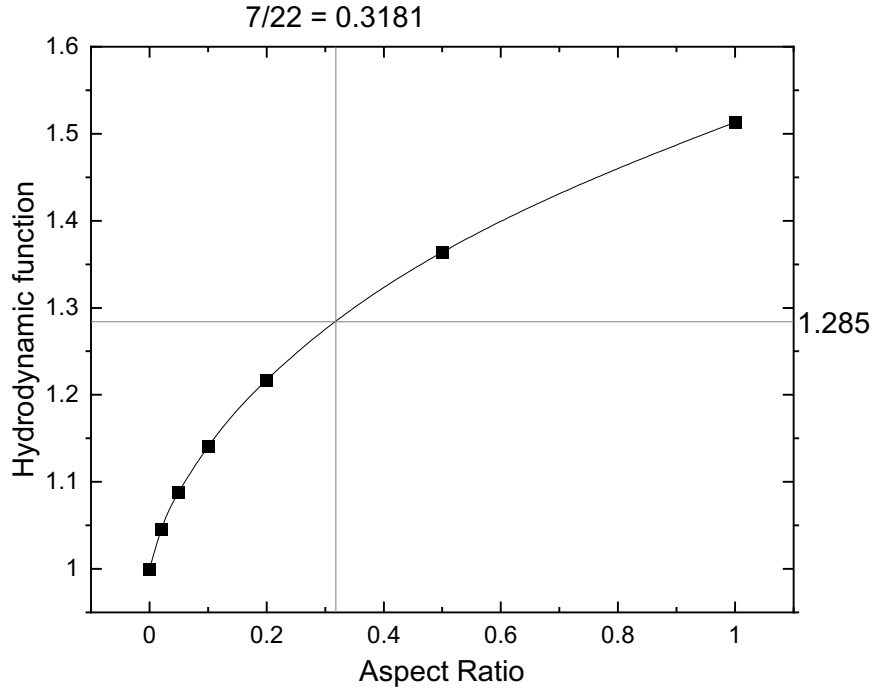
Fig. 4.9: Hydrodynamic function as function of aspect ratio (thickness / width of the wire). Data taken from [34]

Tab. 4.3: Relative change in effective mass $\Delta m_{eff}/m_{eff}$ of MEMS in vacuum and He II as a function of driving voltage.

wire	V_{rms} [V]	$\Delta m_{eff}/m_{eff}$
G1L	0.1	0.06884
G1L	0.23	0.0689
G1R	0.042	0.01964
G1R	0.1	0.01968
G1R	0.23	0.01972
G3R	0.042	0.02004
G3R	0.1	0.02004
G3R	0.23	0.02005

rectangular beam (thickness / width of the wire), see Figure 4.9. For our wires the aspect ratio is 0.31 and the real part of the corresponding hydrodynamic function is 1.285. With this we calculated the theoretical flow enhancement factor as 3.17[2]. Their study was conducted for flows around 2D objects, which can explain a slight difference compared to our experimental results, given in Tab. 4.3.

4.3 Reversal in non-linear effects

At the beginning of this Chapter, we showed that direction of non-linearties changes after reaching a certain driving voltage. In this Section, we will provide

---

[2]Real component of hydrodynamic function represent added apparent mass. Flow enhancement factor was determined using value with definition of hydrodynamic force Eq. (2) from [34] and compared to effective mass of MEMS in vacuum.

a short analysis that will explain the origin of this behavior.

To describe the dynamics of the MEMS, one can use the dynamic Euler-Bernoulli beam theory. Assuming small displacement, the displacement is described by

$$EI\frac{\partial^2 x}{\partial z^4} = -\mu\frac{\partial^2 \omega}{\partial t^2} + q \tag{4.7}$$

where E is elastic modulus and I is the second moment of area of the cross-section of the beam, z is primary coordinate (along the beam), q is force per unit length and μ is the linear mass density. This approach assumes homogeneity of the beam and that E and I are not dependent on z. This approach does not fully describe our problem because displacement is in order of the dimension of the wire. Euler-Bernoulli's beam theory was extended in [32] using Non-Linear Rayleigh Method. They used wires of the same design and similar dimensions; thus, their analytically derived equations can be applied to our case. The non-linearities can have an origin in either the geometry of the wire or an elastic origin. The elastic limit of silicon is in order of several GPa [35]. Our devices experience stresses expressed as

$$\sigma = -zE\frac{d^2 x}{dx^2} \tag{4.8}$$

from the E-B beam theory in the order of MPa. Thus we conclude that we are still in the linear part of the deformation curve. On the other hand thin aluminum layer has a lower elastic limit, and its plasticity may even permanently shift the resonant frequency [32]. This can explain the difference in the resonant frequency of MEMS measured in the previous run 2.2 and in our measurement 3.1.

Geometrical non-linearities in material lead to a change of effective spring constant k_{eff} and effective mass m_{eff} of MEMS in a vacuum. According to Collin et al., [32], the effective parameters for a homogenous beam can be determined using

$$k_{eff} = \frac{3E_z I_z}{h^3}\left(1 - \frac{9t}{4h}\left(\frac{a}{h}\right) + \frac{288}{1120}\left(\frac{a}{h}\right)^2\right) \tag{4.9}$$

$$m_{eff} = \rho V\frac{33}{140}\left(1 - \frac{146190t}{58080h}\left(\frac{a}{h}\right) - \frac{2118666}{1490720}\left(\frac{a}{h}\right)^2\right) \tag{4.10}$$

where E_z is z component of elastic modulus E. a is amplitude of displacement and $V = twh$ is the volume of MEMS. The ratio of these two properties gives the new resonant frequency of the wire, which explains the frequency hardening observed at high drives. In Graph 4.10 we compare experimental and theoretical (black line) frequency shift calculated using Eqs. 4.9 and 4.10. For G1L and G1R wire experimental data agrees well with theory except at the highest amplitude. We suspect that thermal effects may be responsible, as it is difficult to ascertain that the devices are sufficiently thermalized in the high cryogenic vacuum.

The bending of the beam produces stress in the material. This stress is a combination of dissipative and reactive components of stress with respect to the motion of the beam. Specifically, the non-linear reactive component, which oscillates in phase with the wire acceleration, leads to an imbalance of these components, which leads to frequency softening at smaller drives. For higher drives, this effect is negligible in comparison with the geometrical non-linearities discussed above. For more details, see [32].
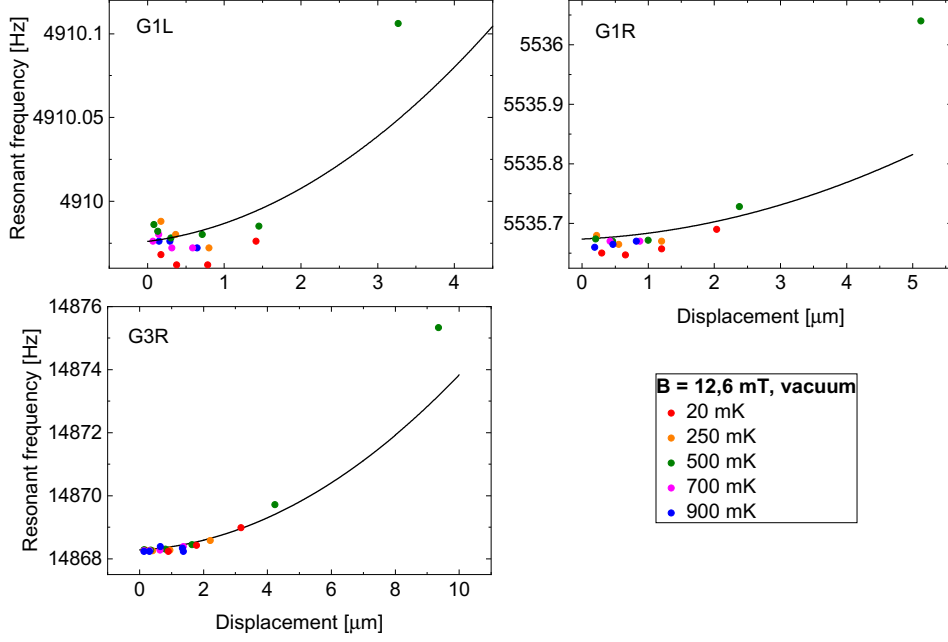
Fig. 4.10: Comparison of experimental and theoretical (black line) frequency shift for all three MEMS.

4.3.1 Transition to resistive state

After reaching critical parameters, thin superconductive layer will transition to resistive state. This would introduce new dissipative effects and thus would change properties of MEMS. Critical current density of thin aluminum in B = 0 is $j_c \approx 7.5 \times 10^{10}$ A/m^2 [36]. Using the cross-section of our devices 154×10^{-12} m^2 we can find its critical current as $I_c = 45$ mA which is several orders more than the highest current flowing in our devices. Thus we conclude that we did not reach resistive phase due to passing of the critical current. Critical magnetic field B_c for 120 nm thick aluminum layer is determined from [37] as $B_c = 60$ mT. Alternative approach of calculating critical field was using Equation 8 from [38] with penetration depth of bulk $\lambda_0 = 5150$ nm and coherent length $\chi = 16000$ nm. This method gives critical magnetic field 94 mT. Critical temperature T_c of bulk aluminum is $T_c = 1.175$ K [39]. This value holds true only for bulk materials and would vary for thin films. Thus we conclude that transition to resistive state occurred due to combination of reaching critical field and critical temperature, which are linked via [15]

$$B_c(T) = B(\text{T} = 0\text{K})\left(1 - \left(\frac{T}{T_c}\right)^2\right). \tag{4.11}$$

Conclusion

In this Thesis, we studied the resonance response of three MEMS devices placed in various homogeneous magnetic fields. MEMS wires were lithographically made with a silicon base and a thin aluminum layer. Aluminum coats were used because they transition to a superconductive phase at temperatures below 1 K. Measurements were conducted at 20 mK, 250 mK, 500 mK, 700 mK and 920 mK. Two MEMS were placed on one micro-chip and measured simultaneously without electrical cross-talk. We began with measurements in a vacuum, and afterwards, we transitioned to experiment in a superfluid helium at a temperature of 20 mK. Even though the experiment ended due to technical issues, it led to these conclusions:

1. Resonant frequency of MEMS change in comparison with the previous measurement. This was explained by crossing the elastic limit in the aluminum layer, leading to a permanent shift in resonance frequencies. The width of the resonance peak was not affected.

2. Measurements in vacuum showed linear amplitude-drive dependency without significant damping. All resonance peaks showed non-linear behavior. Low drive peaks showed frequency softening, and high drive peaks showed frequency hardening. Our measurements were compared to the previous measurement with the same devices but conducted at different magnetic fields. The devices' responses did not quantitatively differ with respect to various magnetic fields with sole exception of measurement at B = 12.6 mT. This behavior was explained by ferromagnetic properties of steel radiation shield in our apparatus.

3. We explained the nonlinear behavior of MEMS. Devices were unaffected by elastic non-linearities because the elastic limit of silicon was not crossed. Elastic non-linearities of the aluminum layer are not the dominant effects; thus, origin of non-linearities lies in the geometry of MEMS. Frequency-softening in low-drive measurement was explained with increased stress in MEMS, leading to an imbalance of dissipative and reactive stress components with respect to the neutral axis. This effect was negligible to the change of effective mass and spring constant of motion of MEMS.

4. Experiments in He II showed that the resonant response of MEMS at higher driving currents is highly damped. We showed that MEMS devices can be used both as generators or as probes of quantum turbulence. We determined the change of effective mass and compared it with the theory. We showed that the flow around the MEMS is accelerated.

5. Increase in resonance line-width in magnetic fields higher that 12.6 mT showed that our devices transitioned to resistive state.

In conclusion MEMS devices can be used in various ways. Firstly they are highly sensitive local probe of quantum turbulence, thus can be used to study complex tangles of quantum turbulence. Another use of MEMS lies in using their motion at higher drives as a source of quntized vortices. In the future we plan

to transition from micro-scale MEMS devices to nano-scale NEMS which should consequently be much more sensitive to quantized turbulence. These devices can be used to trap and measure a single quantized vortex.

Bibliography

[1] Lemeshko, Mikhail & Schmidt, Richard. (2016). Molecular impurities interacting with a many-particle environment: from ultracold gases to helium nanodroplets. 10.1039/9781782626800-00444.

[2] Kapitza, P. Viscosity of Liquid Helium below the λ-Point. Nature 141, 74 (1938). https://doi.org/10.1038/141074a0

[3] ALLEN , J., Misener , A. Flow of Liquid Helium II. Nature 141, 75 (1938). https://doi.org/10.1038/141075a0

[4] Purushothaman, S. (2008). Superfluid helium and cryogenic noble gases as stopping media for ion catchers.

[5] Vinen, W. F., and J. J. Niemela. "Quantum turbulence."Journal of low temperature physics 128 (2002): 167-231

[6] Blaauwgeers, R., Blazkova, M., Človečko, M. et al. Quartz Tuning Fork: Thermometer, Pressure- and Viscometer for Helium Liquids. J Low Temp Phys 146, 537–562 (2007). https://doi.org/10.1007/s10909-006-9279-4

[7] E. Varga, M. J. Jackson, D. Schmoranzer, L. Skrbek, The Use of Second Sound in Investigations of Quantum Turbulence in He II. J. Low Temp. Phys., 197, issue 3-4, (2019).

[8] Pavelyev, A.A., Reshmin, A.I., Teplovodskii, S.K. et al. On the Lower Critical Reynolds Number for Flow in a Circular Pipe. Fluid Dynamics 38, 545–551 (2003)

[9] Kolmogorov, A. N. "The Local Structure of Turbulence in Incompressible Viscous Fluid for Very Large Reynolds Numbers." Proceedings: Mathematical and Physical Sciences, vol. 434, no. 1890, 1991, pp. 9–13. JSTOR,

[10] Joshi, J., & Nayak, A. K. Advances of computational fluid dynamics in nuclear reactor design and safety assessment.2019

[11] U. Frisch. Turbulence: The Legacy of A. N.Kolmogorov. Cambridge University Press, Cambridge, November 1995.

[12] Van Dyke M. An Album of Fluid Motion. Stanford Calif: Parabolic Press; 1982.

[13] Landau LD Lifshits. E. M. Fluid Mechanics.Pergamon Press; 1959

[14] Namburi, Manjusha & Krithivasan, Siddharth & Ansumali, Santosh. (2016). Crystallographic Lattice Boltzmann Method. Scientific Reports. 6. 27172. 10.1038/srep27172.

[15] Ladislav Skrbek a kol., Fyzika Nízkých Teplot. Matfyzpress, (2011). ISBN 978-80-7378-168-2.

[16] Adel, Alyaa & Hassan, Ahmed. (2019). Super uidity properties of 4He using rotating interacting condensate boson as a quantum simulator.

[17] E. L. Andronikashvili, Fiz. Zh. 10, 201 (1946)

[18] C. F. Barenghi, R. J. Donnelly, W.F. Vinen (Eds.), Quantized Vortex Dynamics and Superfluid Turbulence. Springer, (2001). ISBN 978-3-540-45542-4.

[19] L.D. Landau, J. Phys. USSR 5,356(1941)

[20] W. H. Keesom and A. P. Keesom.New measurements on the specific heat of liquid helium Physica 2, 557 (1935).

[21] A. W. Baggaley, J. Laurie, C. F. Barenghi, Phys. Rev. Lett. 109, 205304 (2012)

[22] Vinen, William. (2001). Decay of superfluid turbulence at a very low temperature: The radiation of sound from a Kelvin wave on a quantized vortex. Phys. Rev. B. 64. 10.1103/PhysRevB.64.134520.

[23] Barenghi, C.F., Tsubota, M., Mitani, A. et al. Transient Growth of Kelvin Waves on Quantized Vortices. Journal of Low Temperature Physics 134, 489–494 (2004). https://doi.org/10.1023/B:JOLT.0000012600.81530.6c

[24] D. I. Bradley, D. O. Clubb, S. N. Fisher, A. M. Guénault, R. P. Haley, C. J. Matthews, G. R. Pickett, and K. Zaki, J.Low Temp. Phys. 138, 493 (2005)

[25] Blaauwgeers, R., Blazkova, M., Človečko, M. et al. Quartz Tuning Fork: Thermometer, Pressure- and Viscometerfor Helium Liquids. J Low Temp Phys 146, 537–562 (2007).

[26] Nichol, H. A., et al. Ëxperimental investigation of the macroscopic flow of He II due to an oscillating grid in the zero temperature limit."Physical Review E 70.5 (2004): 056307

[27] J. Jäger, B. Schuderer, and W. Schoepe, Phys. Rev. Lett. 74, 566 (1995)

[28] Marek Talíř. Description of the non-linear oscillators for study of superfluid helium flows. 2022

[29] 2012 BF-H400 User manual, Blue Fors Cryogenics.

[30] Midlik, Š., Sadílek, J., Xie, Z. et al. Silicon Vibrating Micro-Wire Resonators for Study of Quantum Turbulence in Superfluid 4 He. J Low Temp Phys 208, 475–481 (2022).

[31] Steeneken, P.G. & Dolleman, Robin & Davidovikj, Dejan & Alijani, Farbod & Zant, Herre. (2021). Dynamics of 2D Material Membranes.

[32] Collin, E., Filleau, L., Fournier, T. et al. Silicon Vibrating Wires at Low Temperatures. J Low Temp Phys 150, 739–790 (2008).

[33] Childress, Jeff & Liou, Simon & Chien, Chia-Ling. (1988). Magnetic properties of metastable 304 stainless steel with BCC structure.

[34] Douglas R. Brumley, Michelle Willcox, John E. Sader; Oscillation of cylinders of rectangular cross section immersed in fluid. Physics of Fluids 1 May 2010; 22 (5): 052001

[35] https://www.memsnet.org/material/siliconsibulk/ from 28.4.2023

[36] Kuznetsov, V. I., and O. V. Trofimov. "Critical temperatures and critical currents of wide and narrow quasi-one-dimensional superconducting aluminum structures in zero magnetic field."Physica C: Superconductivity and its Applications 595 (2022): 1354030.

[37] R. Meservey, P. M. Tedrow; Properties of Very Thin Aluminum Films. Journal of Applied Physics 1 January 1971; 42 (1): 51–53

[38] Reale, C. Thickness and temperature dependence of the critical magnetic field of thin superconducting films of the aluminium group metals. Acta Physica 37, 53–60 (1974).

[39] Caplan, Sandor, and Gerald Chanin. "Critical-field study of superconducting aluminum."Physical Review 138.5A (1965): A1428.

List of Figures

48

A. Attachments

A.1 First Attachment